

# We are IntechOpen, the world's leading publisher of Open Access books Built by scientists, for scientists

6,900

Open access books available

186,000

International authors and editors

200M

Downloads

Our authors are among the

154

Countries delivered to

TOP 1%

most cited scientists

12.2%

Contributors from top 500 universities



WEB OF SCIENCE™

Selection of our books indexed in the Book Citation Index  
in Web of Science™ Core Collection (BKCI)

Interested in publishing with us?  
Contact [book.department@intechopen.com](mailto:book.department@intechopen.com)

Numbers displayed above are based on latest data collected.  
For more information visit [www.intechopen.com](http://www.intechopen.com)



# Design of High Performance and Low-Cost Single Longitudinal Mode Laser Module for DWDM Application

Huei-Min Yang

*I-Shou University/Communication Engineering Department  
Taiwan*

## 1. Introduction

Over the past years, the internet core rapidly increases, transparent protocols become more available for DWDM system in the fiber to the home, fiber to the institutions service. In densely spaced wavelength-routed and large-capacity optical network systems, single-mode lasers with narrow linewidth and low temperature sensitivity are of particular importance as the light sources in transmitter modules. The efficient coupling of a laser diode to an optical fiber has been a problem of general concern since the advent of fiber-optic communication systems. This chapter will introduce to fabricate a fiber grating external cavity laser (FGECL) module with a low cost while still maintaining a good single longitudinal mode performance by using a low-cost AR(Anti-reflection)-coated( $5 \times 10^{-3}$ ) laser and a tapered hyperbolic-end fiber (THEF) microlens for strong coupling the fiber grating external cavity. Previously, high-performance FGECL modules have only been available by using a complicated AR-coated( $1 \times 10^{-5}$ ) laser process that leads to a high packaging cost. The FGECL consisted of a HR/AR-coated diode laser, an uncoated THEF microlens, and a fiber grating. The results showed that the FGECL module exhibits a side-mode suppression ratio (SMSR) higher than 44 dB, a higher output power of more than 2 mW, and a larger operation current range of over 50 mA. In addition, excellent wavelength stability and a low-penalty directly modulated 2.488 Gbit/s were also obtained for FGECL modules. The THEF microlens demonstrated up to 86% coupling efficiency for a laser with an aspect ratio of 1:1.5. A fiber microlens which provides an efficient coupling mechanism to match the spot size of the diode laser to the fiber is commonly used for optical alignment in FGECL modules. Low-cost FGECL modules with good performance were achieved primarily owing to the THEF microlens having a high coupling efficiency (typically 75%) which enhanced the feedback power from the fiber grating external cavity to the HR/AR-coated laser compared with the currently available hemispherical microlens which has low coupling efficiency (typically 50%). Therefore, the packaged FGECL module is suitable for use in low cost 2.5 and 10 Gbit/s lightwave transmission systems, such as gigabit passive optical networks (GPONs), metropolitan area networks (MANs), and fiber-to-the-home (FTTH) applications.

This chapter is organized as follows:

Part I: A tapered hyperbolic-shaped microlens has been improved for efficient the coupling of the output from a laser diode into an optical fiber. A tapered hemispherical-end

fibermicrolens is also evaluated for comparison purposes. The Fresnel diffraction theory is used to evaluate laser to fiber coupling using microlenses. Experimental results demonstrate that, for an elliptical Gaussian laser diode with an aspect ratio of 1:1.5, the coupling efficiencies for the hyperbolic-shaped microlenses and the hemispherical-end fiber microlenses are 87% and 62%, respectively. Calculation results show excellent agreement with the measurements. The research results illustrate that a hyperbolic-shaped microlens has a much higher coupling efficiency than a hemispherical-end microlens due to efficient mode matching and phase matching. An empirical model and a comparison of coupling efficiency between hyperbolic-end and hemispheric-end microlenses are presented.

Part II describes a new scheme of the tapered hyperbolic-end fiber (THEF) and experimental setup. A new lensed-fiber scheme for producing a THEF microlens with an efficient coupling between a laser diode and a single-mode fiber. The high-coupling performance of microlenses with a hyperbolic profile was due to the improved mode matching between the laser and the fiber when compared to currently available hemispherical microlenses. The THEF microlens is ideally suited to collect all the available radiation emitting from a laser source. The diffraction theory predicted that near 100% coupling efficiency could be achieved by a THEF with a circular laser beam pattern, based on both the horizontal and vertical far-field angles of 20 degrees.

Part III describes a low-cost FGECL modules with good performance which were achieved primarily owing to the THEF microlenses having a high coupling efficiency (typically 75%). In general, a high-performance FGECL requires a low AR-coated ( $1 \times 10^{-5}$ ) laser. However, such packages require complicated processes, which make their cost too high. Using a temperature-insensitive and low-chirp fiber Bragg grating reflector as the external cavity for the semiconductor gain element. The possibility fabricating FGECL modules at low cost while still maintaining a good performance by employing a low-cost AR-coated ( $5 \times 10^{-3}$ ) laser and a THEF microlens can be demonstrated in the part III. The fiber grating external cavity lasers (FGECLs) have been developed for 2.5 Gbit/s WDM with a low bit error rate penalty. It has been shown that the side-mode suppression ratio (SMSR) of the non-AR-coated FGECL exhibits a current-dependent oscillation.

## 2. Theoretical fundamentals between a tapered hyperbolic-shaped microlens and a hemispherical-end fiber microlens

A hyperbolic-shaped microlens, the shape of a perfect microlens was modeled in the shape of a hyperbolic curve, which was different from the previous studies. The hyperbolic-shaped microlens of this study transforms accurately the incident Gaussian pattern wave into a plane wave according to geometric optics. The novel hyperbolic-shaped microlenses were fabricated by symmetrically tapering the fibers during the unique etching process and hyperbolically lensing the tips during the fusing process. In comparison with other techniques of making hyperbolic-shaped microlenses, the fabrication process of our tapered hyperbolic-shaped fiber microlens is reproducible and suitable for high-volume production.

### 2.1 A model of the hemispherical-end microlens

Fig. 1(a) shows the hemispherical-end microlens with a radius of curvature of  $9.4 \mu\text{m}$ . The equation for the hemispherical-end microlens can be expressed as Eq. (1)

$$(R_\ell - z)^2 + r^2 = R_\ell^2 \quad (1)$$

where  $z$  is the axial coordinate along the optical axis of the lens (the direction of traveling wave),  $r$  is perpendicular to the optical axis,  $R_\ell$  is one radius of curvature of the hemispherical-end microlens, as shown in Fig. 1(b). The phase transformations of the hemispherical-end microlens can be expressed as Eq. (2)

$$t_\ell(r) = \exp\left[-i \cdot \kappa \cdot (n - 1) \cdot \left(R_\ell - \sqrt{R_\ell^2 - r^2}\right)\right] \quad (2)$$

where  $n$  is the refractive index of the fiber core and  $\kappa$  represents the wave number of a propagating wave, given by  $2\pi/\lambda$ . The Gaussian laser beam entering into the mode field of the hemispherical-end microlens can be stated as Eq. (3)

$$U_n(x, y, z) = U_{sx}(x, z) \cdot U_{sy}(y, z) \cdot t_\ell(r) \quad (3)$$

with Eqs. (1), (2) and (3), we can calculate the coupling efficiency of an elliptical Gaussian mode laser to the hemispherical-end microlens.

### 2.2 A model of the hyperbolic-shape microlens

The lens shape of a perfect the hyperbolic-shape microlens was modeled by a hyperbolic curve. Fig. 2(a) shows the hyperbolic-shape microlens with a radius of curvature of  $9.4 \mu\text{m}$  and the simulated hyperbolic curve from the enlarged tip. The feature of the hyperbolic-shape microlens has a smaller taper angle than the hemispherical-end microlens and a larger tilt taper angle of the lens tip of the hyperbolic-shape. The hyperbolic equation can be expressed as

$$\frac{z^2}{a^2} - \frac{r^2}{b^2} = 1 \quad (4)$$

This formula was derived from the fitted lens radius,  $R_\ell$ , within the core region and the tilt angle,  $\theta_a$ , of the asymptotic line with respect to the fiber axis, where  $z$  is the axial coordinate along the optical axis of the lens (i.e. the direction of traveling wave),  $r$  is perpendicular to the optical axis and is equal to the square root of  $x^2 + y^2$ , as shown in Fig. 2(b).

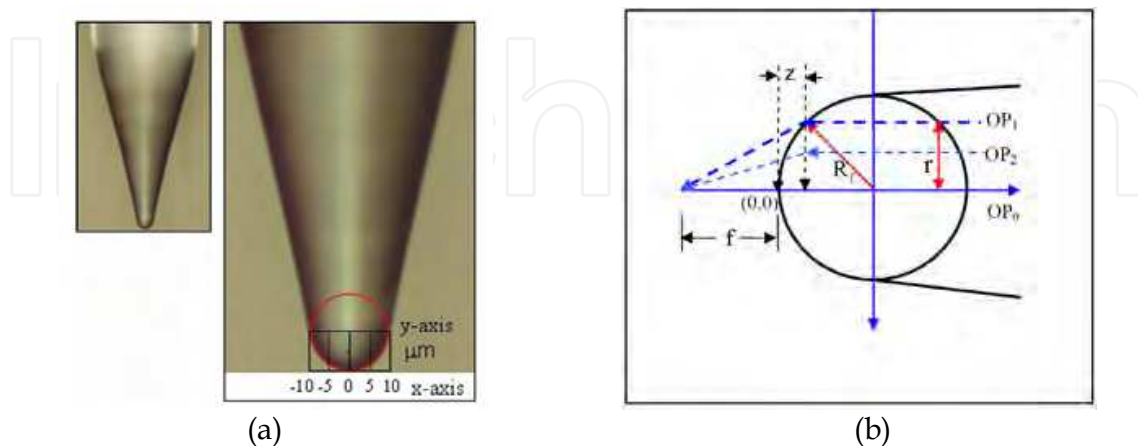


Fig. 1. (a) Hemispherical-end microlens with a radius of curvature of  $9.4 \mu\text{m}$ , right figure is a simulated hemispherical curve from the enlarged tip. (b)  $z$  is the axial coordinate along the optical axis of the lens (the direction of traveling wave), and  $r$  is perpendicular to the optical axis.

We assume that the circle was fitted perfectly within the fiber core region. The repeatability of the measurement is within 1 $\mu$ m. Hence, the center point, (h, 0), of the circle can be calculated with the following equation,

$$h(a) = r_f^2 \cdot \frac{\left[ \frac{1}{\tan(\theta_a)^2} + 1 \right]}{2 \cdot \left[ \sqrt{\left[ \frac{r_f^2}{\tan(\theta_a)^2} + a^2 \right]} - a \right]} \quad (5)$$

where  $r_f$  is the fiber core radius. Since the following equation needs to be satisfied,

$$R_\ell + a - h(a) = 0 \quad (6)$$

$R_\ell$  is one radius of curvature of the hyperbolic-shape microlens, the value of  $a$  can be solved in terms of the measured parameters. The value of  $b$  is calculated from the asymptotic relationship,

$$b = a \cdot \tan(\theta_a) \quad (7)$$

The phase transformations for the hyperbolic lens can be represented by the following equations (8) & (9)

$$t_{\ell_x}(x) = \exp \left[ -i \cdot \kappa \cdot (n-1) \cdot \left( \frac{a}{b} \cdot \sqrt{b^2 + (x+d_x)^2} - a \right) \right] \quad (8)$$

$$t_{\ell_y}(y) = \exp \left[ -i \cdot \kappa \cdot (n-1) \cdot \left( \frac{a}{b} \cdot \sqrt{b^2 + (y+d_y)^2} - a \right) \right] \quad (9)$$

where  $n$  is the refractive index of the fiber core, and  $d_x$  and  $d_y$  represent the deviation (offset) of the lens from the fiber center axis in the horizontal and vertical directions, respectively. The mode field after the hyperbolic-shape microlens can be expressed as

$$U_n(x, y, z) = U_{sx}(x, z) \cdot U_{sy}(y, z) \cdot t_{\ell_x}(x) \cdot t_{\ell_y}(y) \quad (10)$$

### 2.3 Experiments and analysis of transmission properties

The laser-to-fiber coupling was modeled based on the Fresnel diffraction theory. From the elliptical Gaussian laser source to the fiber microlens, which used Fresnel diffraction for beam propagation through the free space. At the lens tip, a phase delay caused by the fiber microlens was added to the electric field. Finally, an overlap integral between the transformed field and the fiber mode field was calculated to obtain a coupling efficiency.

The mode field patterns for both the laser and fiber were assumed to be Gaussian and the 1550 nm laser diode had an elliptical emission pattern. The measured full-width-half-maximum (FWHM) far-field angles along the horizontal and vertical directions,  $\theta_x$  and  $\theta_y$ , were used to calculate the laser mode-field radii at the front facet,  $\omega_{0x}$  and  $\omega_{0y}$ , respectively. The relationship between the far-field angle and the mode-field radius at the waist can be derived as

$$\omega_{0x} = \left( \sqrt{\ln(2)/2} \right) \lambda / \left( \pi \cdot \tan(\theta_x/2) \right) \quad (11)$$

$$\omega_{oy} = \left( \sqrt{\ln(2)/2} \right) \lambda / \left( \pi \cdot \tan(\theta_y/2) \right) \quad (12)$$

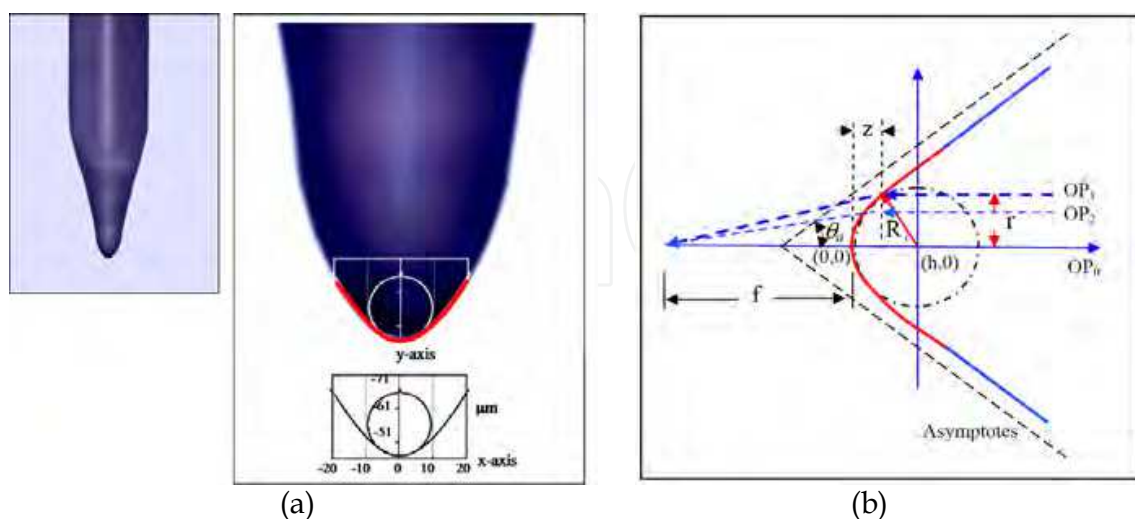


Fig. 2. (a) Enlarged tip of hyperbolic-shape microlens with a radius of curvature of 9.4 μm. (b) The circle was fitted perfectly within the fiber core region, z is the axial coordinate along the optical axis of the lens, r is perpendicular to the optical axis, the tilt angle of the asymptotic line with respect to the fiber axis with θ<sub>a</sub>.

The laser mode fields at a distance Z from the facet were thus represented by the Fresnel diffraction theory,

$$U_{sx}(x, z) = \int_{-\infty}^{\infty} \exp \left[ -\left( x_1 / \omega_{ox} \right)^2 + i \cdot (\kappa / 2 \cdot z) \cdot (x - x_1)^2 \right] dx_1 \cdot \sqrt{\exp(i \cdot \kappa \cdot z) / (i \cdot \lambda \cdot z)} \quad (13)$$

$$U_{sy}(y, z) = \int_{-\infty}^{\infty} \exp \left[ -\left( y_1 / \omega_{oy} \right)^2 + i \cdot (\kappa / 2 \cdot z) \cdot (y - y_1)^2 \right] dy_1 \cdot \sqrt{\exp(i \cdot \kappa \cdot z) / (i \cdot \lambda \cdot z)} \quad (14)$$

where λ is the wavelength, and κ is the wave number, given by 2π/λ. Equations (13) and (14) do not include the astigmatism for the laser diode. This is the case for the well-designed index-guided lasers. Finally, the coupling efficiency is calculated from the overlap integral of this new mode field with the fiber fundamental mode field, U<sub>f</sub>(x, y),

$$\eta(z) = \frac{\left| \int_{-\infty}^{\infty} \int_{-\infty}^{\infty} U_n(x, y, z) \cdot U_f^*(x, y) dx dy \right|^2}{\int_{-\infty}^{\infty} \int_{-\infty}^{\infty} U_n(x, y, z) \cdot U_n^*(x, y, z) dx dy \cdot \int_{-\infty}^{\infty} \int_{-\infty}^{\infty} U_f(x, y) \cdot U_f^*(x, y) dx dy} \quad (15)$$

For a fixed fiber lens radius, the coupling efficiency between the laser diode and the fiber was calculated. The hyperbolic-shape microlenses had a much higher coupling efficiency than the hemispherical-end microlenses for an elliptical Gaussian laser with an aspect ratio of 1:1.5. An experimental comparison of the hyperbolic-shape microlenses has demonstrated a coupling efficiency of up to 86.8% while the hemispherical-end fiber microlenses with taper asymmetry have demonstrated imperfect coupling of at best

61.5%. An elliptical Gaussian laser diode with an aspect ratio of 1:1.5, a widely adopted commercial product, has a full-width-half-maximum (FWHM) far-field divergence of  $20^\circ \times 30^\circ$  (lateral  $\times$  vertical) at  $20^\circ\text{C}$  and 60 mA, both horizontal angle and vertical angle as shown in Figs. 3(a) and (b), respectively. Theoretically, a high coupling efficiency can be obtained under specific conditions, for example, the coupling loss is relative to the radii of curvature of microlenses and laser diodes aspect ratio. The diffraction theory predicted that near 100 % coupling efficiency could be achieved by a hyperbolic-shape microlens with a circular laser beam pattern, based on both the horizontal and vertical far-field angles of 20 degrees.

Fig. 4 shows the coupling efficiency as a function of radius of curvature for a laser diode with an aspect ratio of 1:1.5; the hyperbolic-shape microlenses can reach a 95% coupling efficiency and the hemispherical-end fiber microlenses with a typical coupling efficiency of only 70% for calculation results. The theory does not take into account any astigmatism in the endface of the fiber microlens. There is a difference in optical field distributions between an elliptical Gaussian laser diode and the radius of curvature, not only in the size, but also in the profile. The coupling loss of a spot-size transformation between the tapered hyperbolic-shape fiber lens and an elliptical Gaussian laser diode is extremely reduced by controlling the shape of the hyperbolic lens tapered portion. The hyperbolic-shape microlenses have a higher coupling efficiency due to larger acceptance angles which was the major reason to bring about excellent mode matching, as shown in Fig. 5.

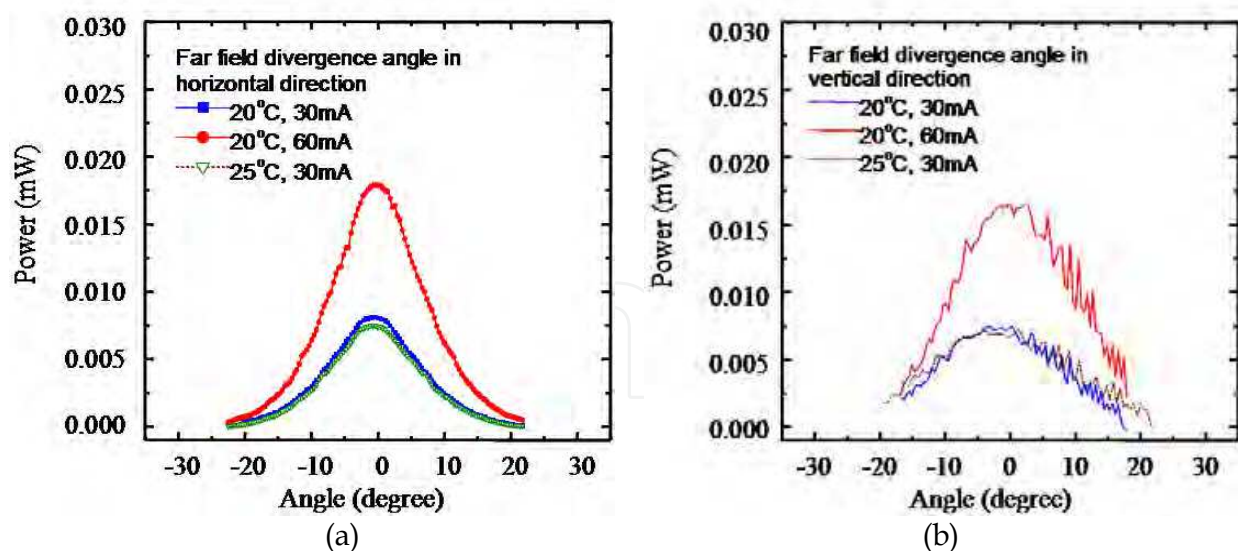


Fig. 3. An elliptical Gaussian laser diode with an aspect ratio of 1:1.5 has a full-width-half-maximum (FWHM) far-field divergence of  $20^\circ \times 30^\circ$  (lateral  $\times$  vertical) at  $20^\circ\text{C}$  and 60 mA (a) horizontal direction and (b) vertical direction.

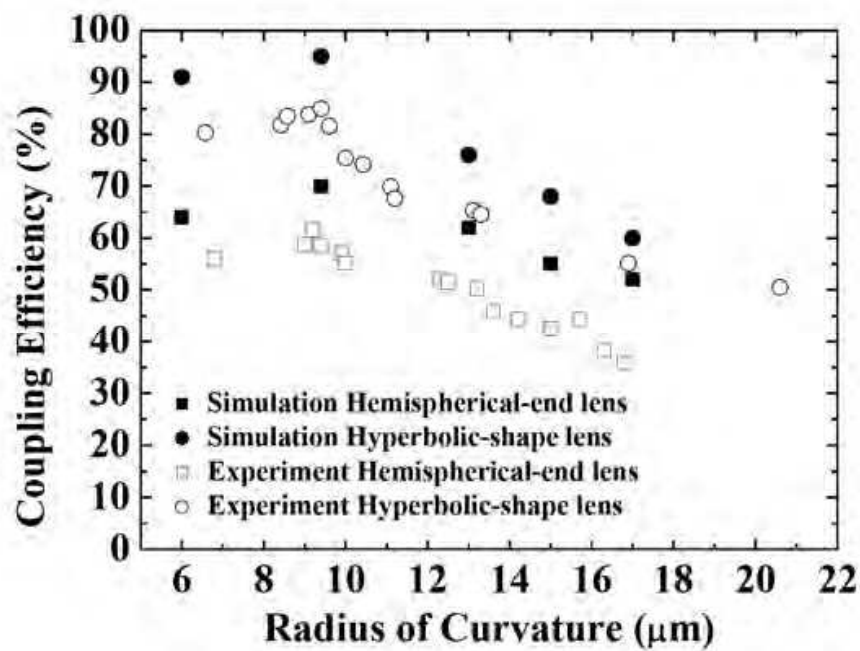


Fig. 4. The coupling efficiency as a function of radius of curvature for a laser diode with an aspect ratio of 1:1.5, the coupling loss is relative to the radii of curvature of microlenses and laser diodes aspect ratio. The hyperbolic-shape microlenses have a much higher coupling efficiency than the hemispherical-end microlenses for experimental and calculated results.

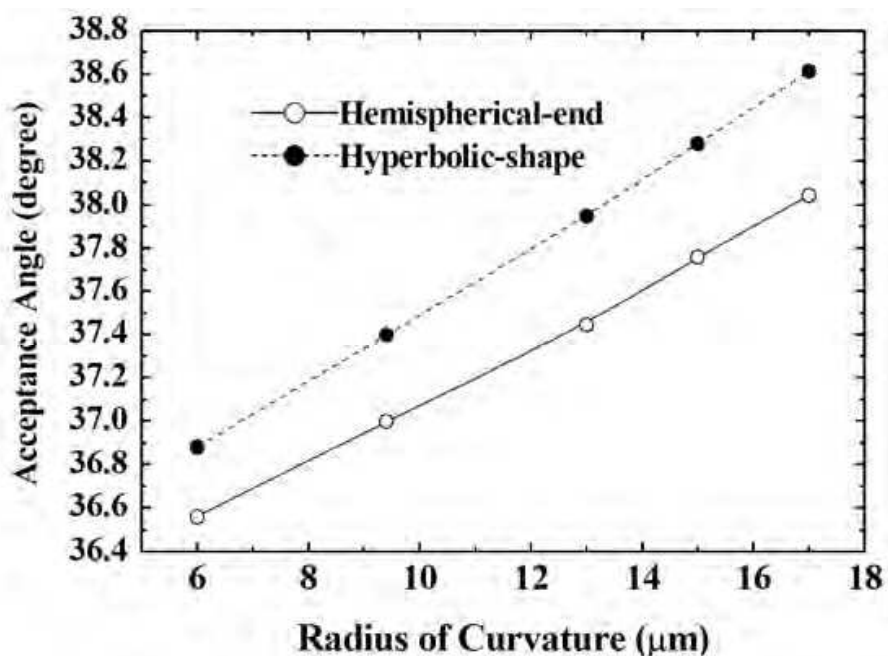


Fig. 5. Hyperbolic-shape microlenses have a higher coupling efficiency due to larger acceptance angles than the hemispherical-end microlenses.

For calculating the intensity and wavefront inside the optical waveguide, we have designed two models of the hyperbolic-shape and the hemispherical-end microlens with Solidworks software, as shown in Fig. 6. Figs. 6(a-1) and (a-2) show the pictures of the hemispherical-end microlens and an enlarged tip, respectively. Figs. 6(b-1) and (b-2) show the hyperbolic-shape microlens and an enlarged tip, respectively. Figs. 7(a) and (b) show the optical intensity and the two-dimensional contour plots at  $4.7 \mu\text{m}$  from the tip of microlens in the optical waveguide of the hemispherical-end microlenses and the hyperbolic-shape microlenses, respectively; both microlenses were of a radius curvature of  $9.4 \mu\text{m}$  and the beam was propagating along the z-direction (the fiber axis). Figs. 8(a) and (b) show the optical intensity and the two-dimensional contour plots at  $18.8 \mu\text{m}$  from the tip of microlens in the optical waveguide of the hemispherical-end microlenses and the hyperbolic-shape microlenses, respectively. Obviously, the hyperbolic-shape microlens shows a strengthened intensity along the waveguide path after transformation by the microlens. The optical intensity of the hyperbolic-shape microlenses with radii of curvature were of  $9.4 \mu\text{m}$  and  $15 \mu\text{m}$  at  $4.7 \mu\text{m}$  from the tip of microlens in the optical waveguide, the strengths were  $0.933 \text{ a.u.}$  and  $0.789 \text{ a.u.}$ , respectively, as shown in Figs. 9(a) and (b), respectively. Therefore, a radius of curvature of  $9.4 \mu\text{m}$  is an optimal lens of the hyperbolic-shape microlenses of standard single-mode fibers owing to higher coupling efficiencies after lenses' transformation. The calculation of the effect of the optical coupling of the hyperbolic-shape microlenses based on an empirical model is in agreement with the measured results.

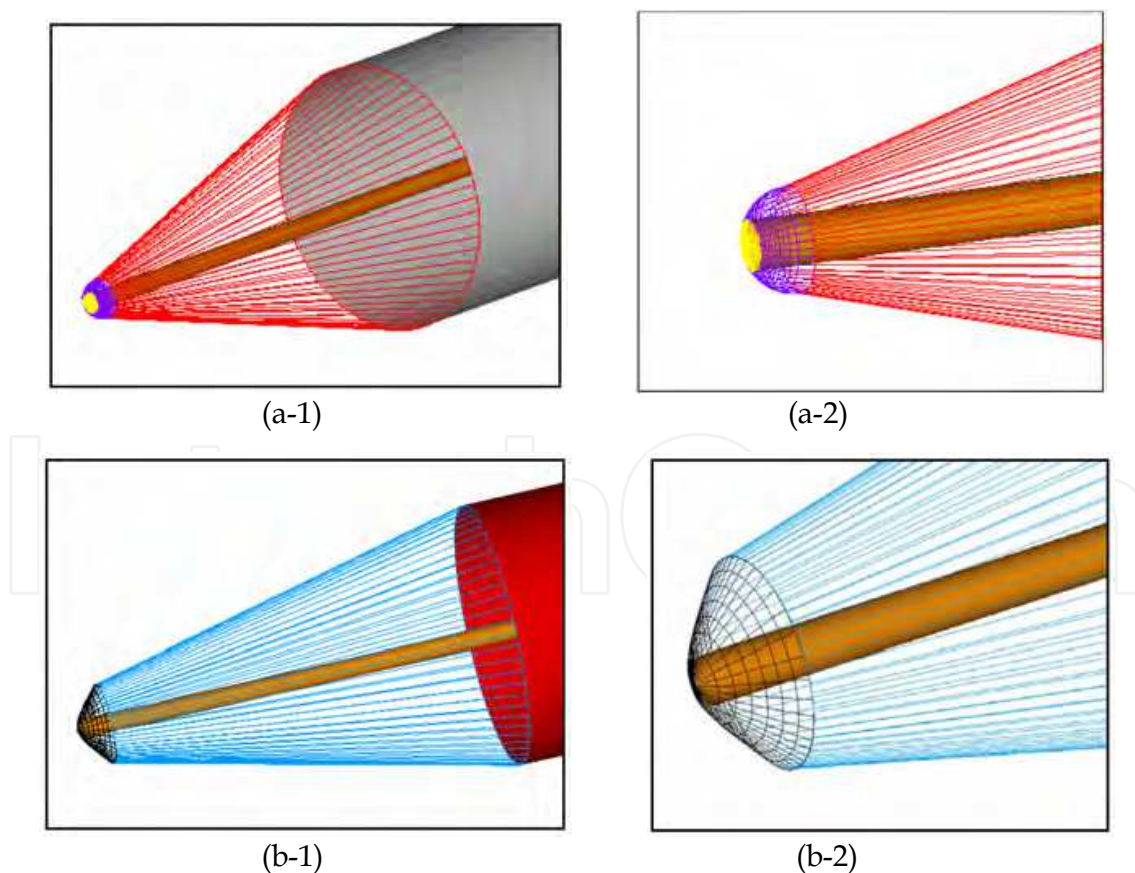


Fig. 6. Two models with Solidworks software, (a-1) hemispherical-end microlens, (a-2) enlarged tip of the hemispherical-end microlens, and (b-1) hyperbolic-shape microlens, (b-2) enlarged tip of the hyperbolic-shape microlens.

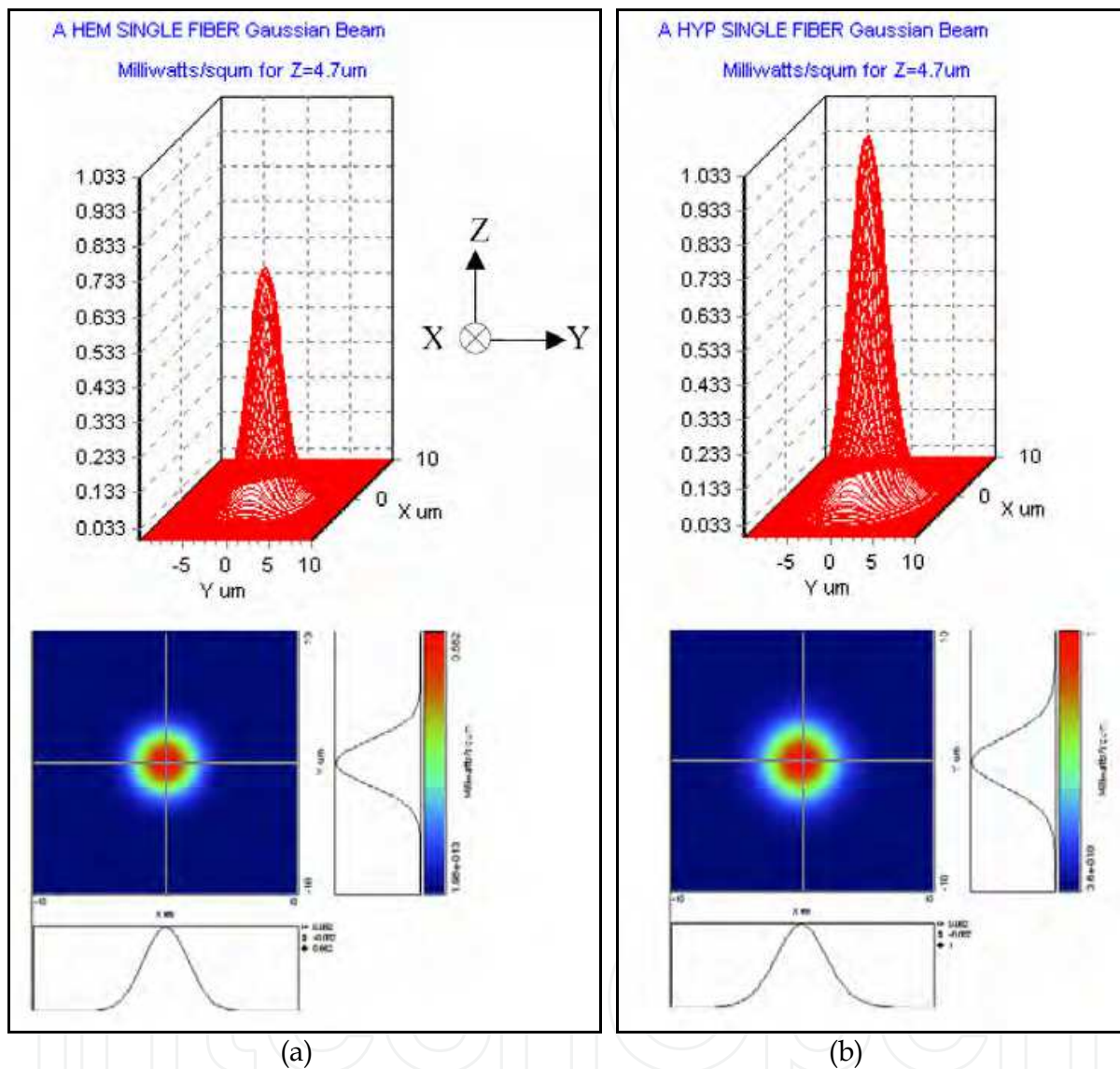


Fig. 7. The optical intensity and the two-dimensional contour plots at  $4.7\mu\text{m}$  from the tip of microlens in the optical waveguide. Both the hyperbolic-shape and the hemispherical-end microlens were of a radius curvature of  $9.4\mu\text{m}$ , the beam was propagating along the z-direction (the fiber axis). (a) hemispherical-end microlens, and (b) hyperbolic-shape microlens.

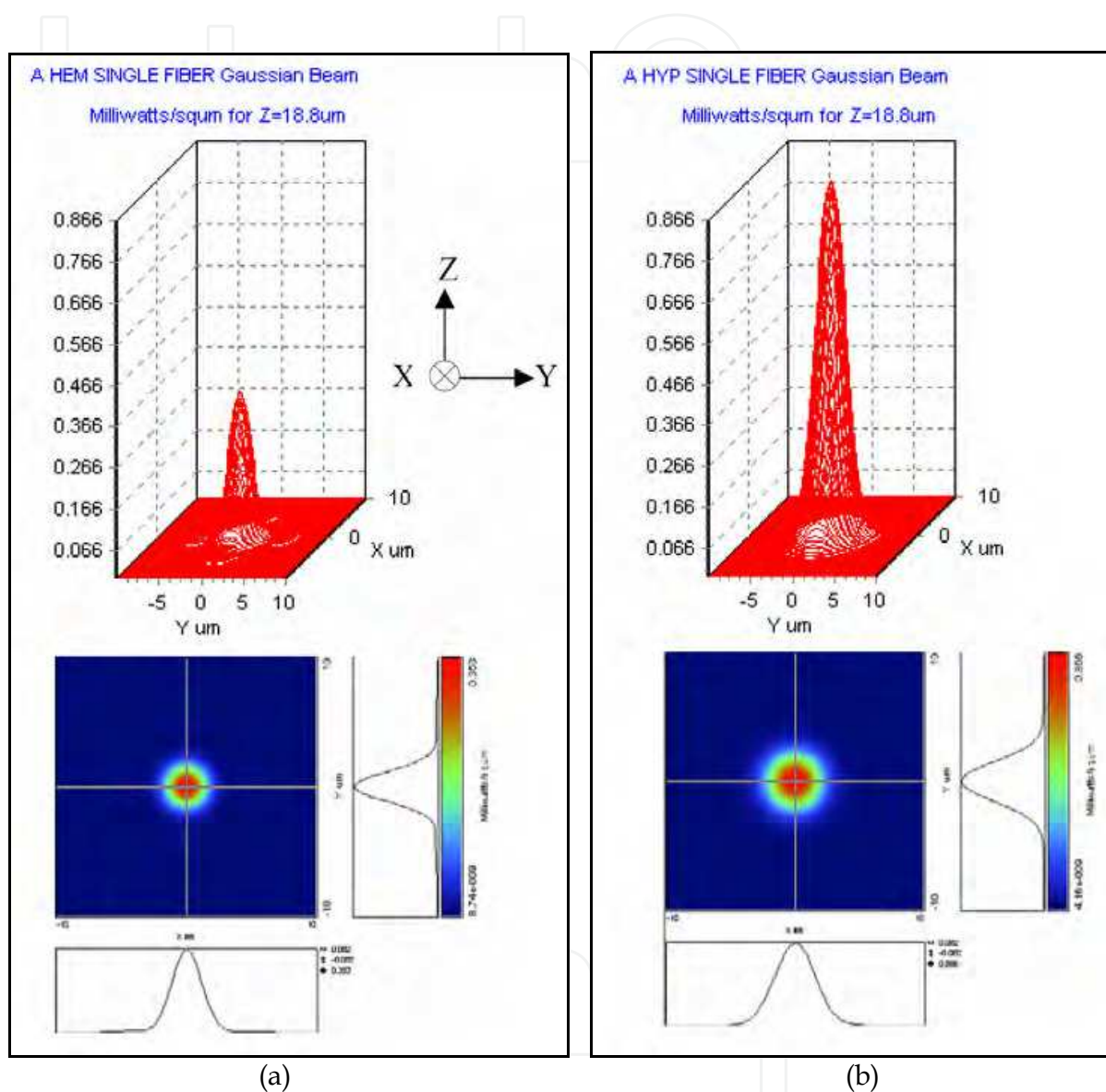


Fig. 8. The optical intensity and the two-dimensional contour plots at  $18.8 \mu\text{m}$  from the tip of microlens in the optical waveguide. Both the hyperbolic-shape and the hemispherical-end microlens were of a radius curvature of  $9.4 \mu\text{m}$ , the beam was propagating along z-direction (the fiber axis). (a) hemispherical-end microlens, and (b) hyperbolic-shape microlens.

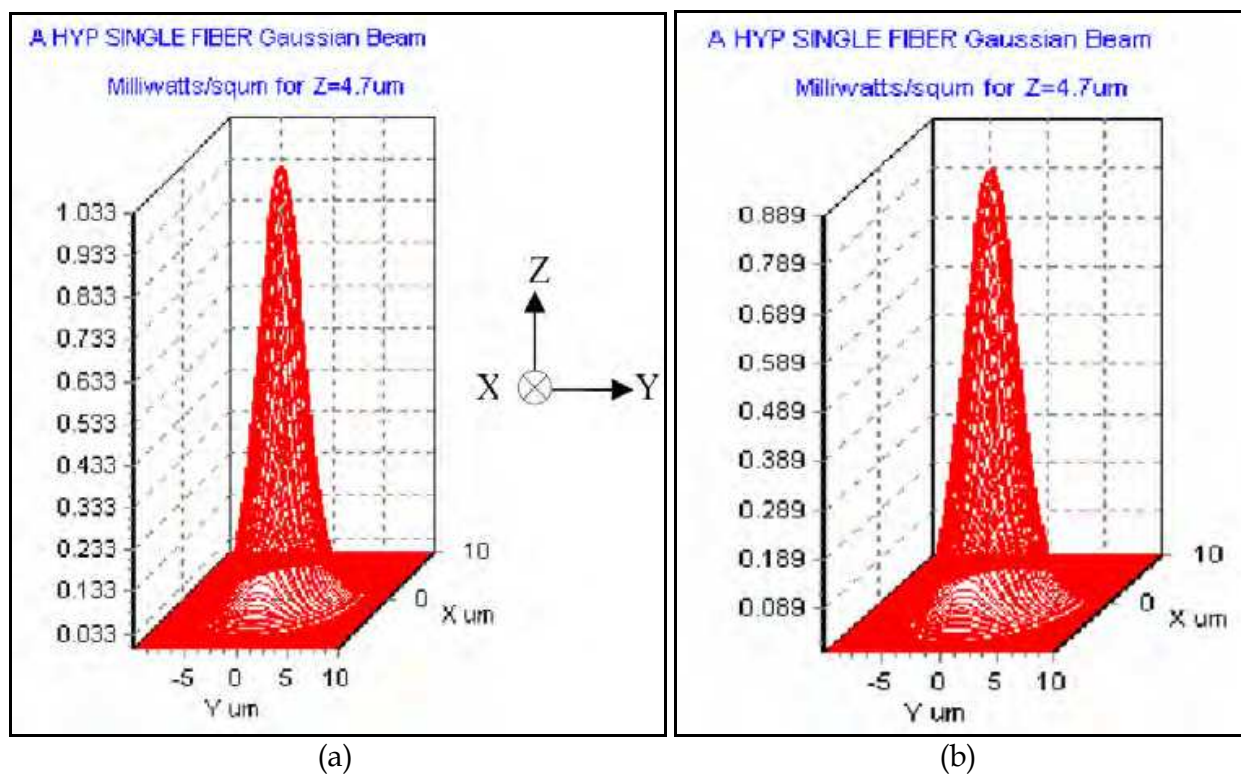


Fig. 9. Optical intensity of the hyperbolic-shaped microlenses 4.7  $\mu\text{m}$  from the tip of the microlens in the optical waveguide. The strengths were (a) 0.933 a.u. with curvature radius of 9.4  $\mu\text{m}$  and (b) 0.789 a.u. with a curvature radius of 15  $\mu\text{m}$ .

Fig. 10(a)-(c) show the variation of wavefronts at the different distances from the tip of microlens in the optical waveguide, of 1.1471, 4.7, 50  $\mu\text{m}$ , respectively. The wavefronts of the hemispherical-end microlenses aren't in accordance with the Gaussian shape in the optical waveguide due to the existence of radiation modes and a greater Fresnel's reflections on the endface of the lens tip. From numerical results with a radius curvature of 9.4  $\mu\text{m}$ , the hyperbolic-shape microlenses have less normalized phase aberration than the hemispherical-end microlenses with wavelength of 1.55  $\mu\text{m}$ , as shown in Fig. 11. It was evidenced in the phase matching after microlens's transformation of the hyperbolic-shape microlens which was not that of the hemispherical-end microlens. From both of the simulations and experiments, the hyperbolic-shape microlenses can be proved with a much better coupling efficiency than the hemispherical-end microlenses, due to phase matching between the Gaussian type laser source and the fiber mode. In addition to the wavefront matching between the propagating laser beam and the fiber mode, the spot-size matching of the Gaussian field distribution is a major reason of improving the coupling efficiency for the hyperbolic-shape microlenses. Compared to the near field intensity patterns, 1  $\mu\text{m}$  of near the tip of lens in free space, both the hyperbolic-shape microlens and the hemispherical-end microlens with a radius curvature of 9.4  $\mu\text{m}$  are shown in Figs. 12(a) and (b). Obviously, the hyperbolic-shape microlenses, as shown in Fig. 12 (b), have much stronger optical intensity and a larger extent of an elliptical field than the hemispherical-end microlenses.

We have compared the optical transformation of the hyperbolic-shaped microlens versus the hemispherical-end microlens for efficient coupling to an elliptical Gaussian laser diode of aspect ratio 1:1.5. The coupling efficiencies for both the tapered hyperbolic-shaped

microlens and a tapered hemispherical-end fiber microlens were calculated based on the Fresnel diffraction theory and the results are in good agreement with the measurements. From the theoretical calculations, we show that uncoated tapered hyperbolic-shaped microlenses, affected solely by Fresnel's reflections, suffer less than 0.2 dB loss when coupled to an elliptical Gaussian mode laser of aspect ratio 1:1.5.

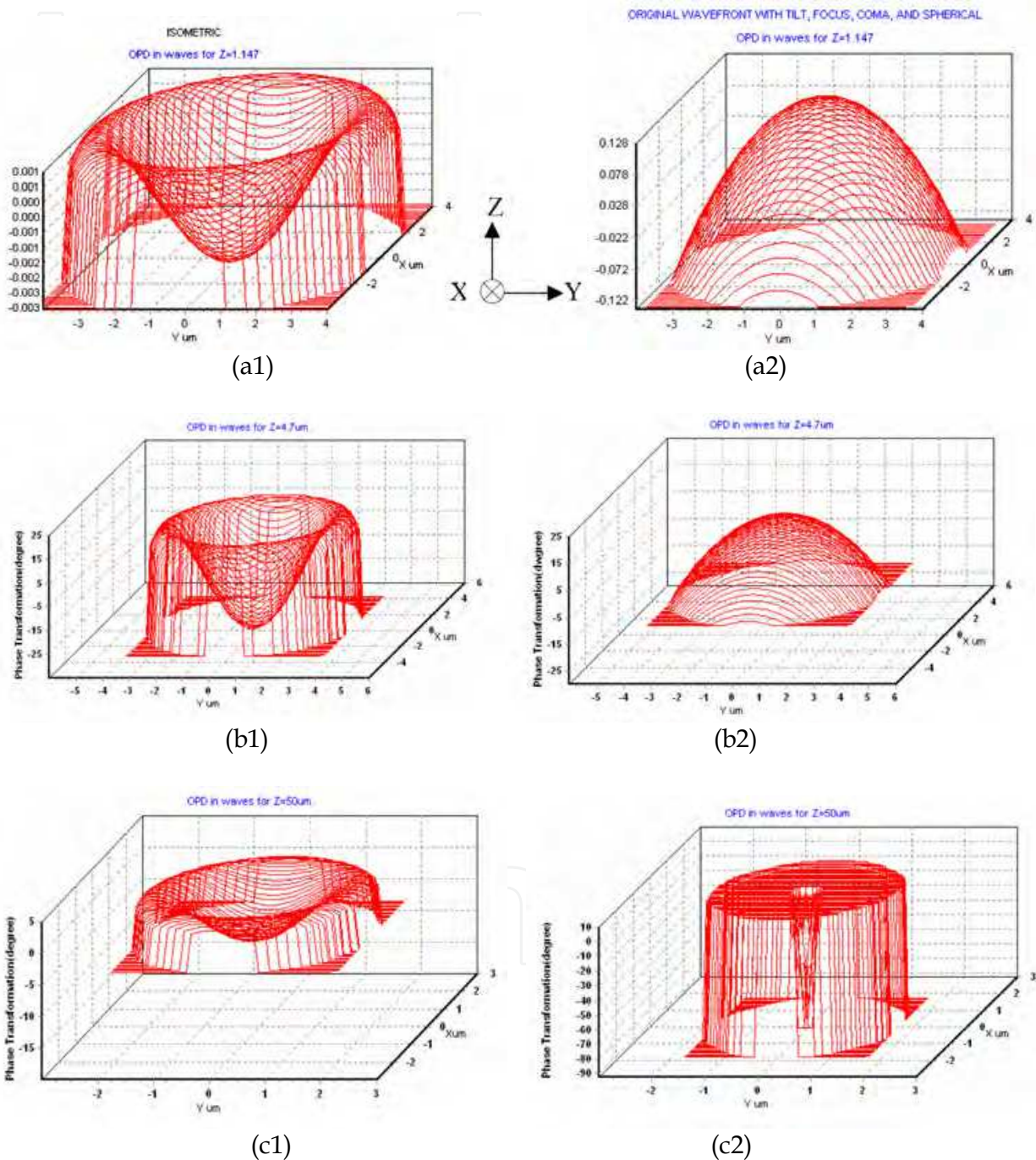


Fig. 10. The variation of wavefronts at the different distances from the tip of microlens in the optical waveguide at (a) 1.1471  $\mu\text{m}$ , (b) 4.7 and (c) 50  $\mu\text{m}$ , respectively. (a-1), (b-1) and (c-1) are for hemispherical-end microlenses. (a-2), (b-2) and (c-2) are for hyperbolic-shaped microlenses.

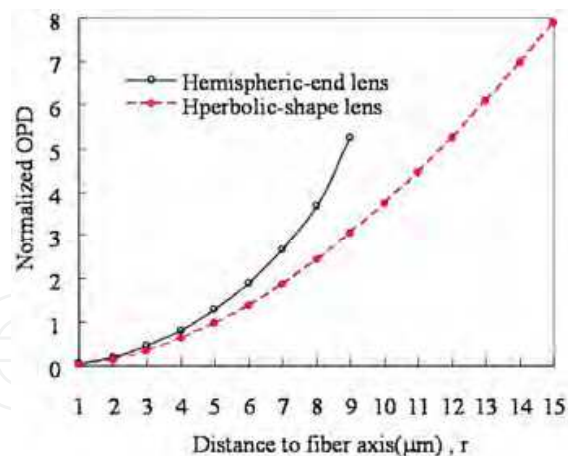


Fig. 11. For the hemispherical-end and the hyperbolic-shaped microlenses of curvature radius  $9.4 \mu\text{m}$ , the hyperbolic-shaped microlenses have a less normalized phase aberration at wavelength  $1.55 \mu\text{m}$ .

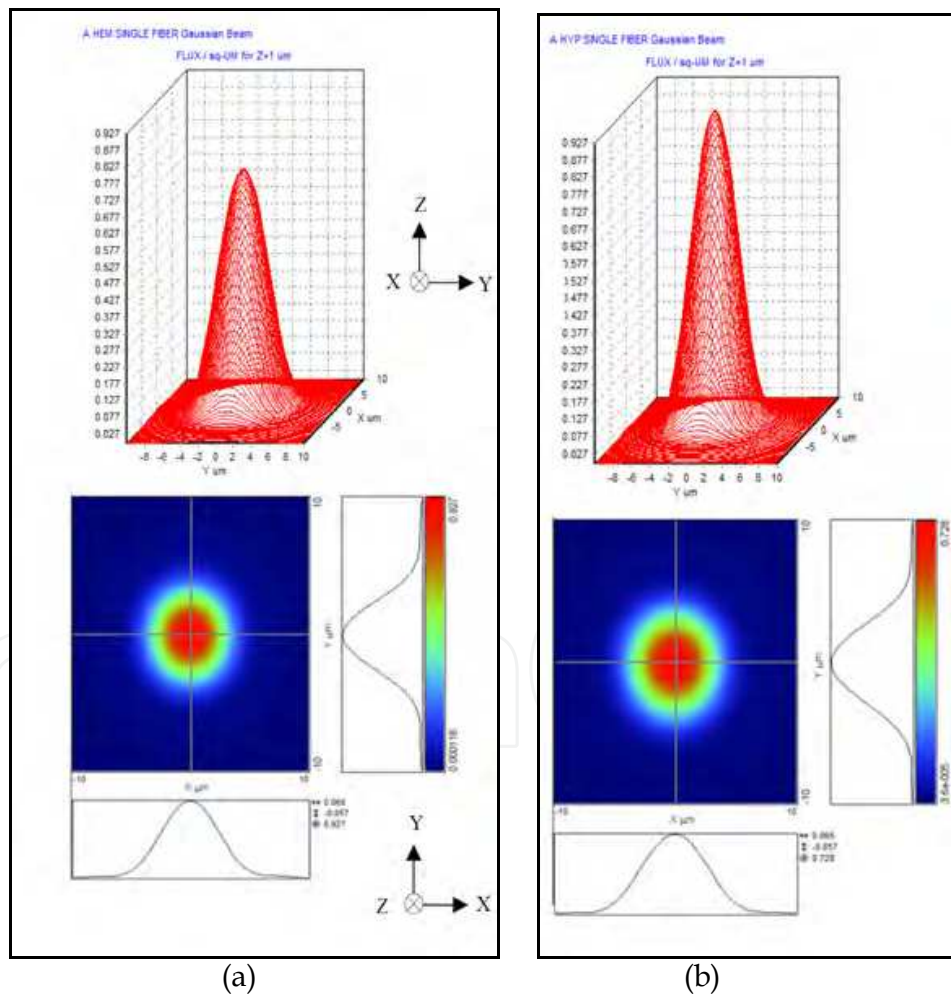


Fig. 12. Near field intensity patterns for: (a) hemispherical-end microlens and (b) hyperbolic-shaped microlens  $1 \mu\text{m}$  near the tip of the lens. Both the hyperbolic-shaped microlenses and the hemispherical-end microlenses are of curvature radius  $9.4 \mu\text{m}$ . The hyperbolic-shaped microlens shows a larger extent of the elliptical field.

### 3. Manufacturing process of fiber microlenses

The fibers used in this discuss were Corning step-index single-mode fibers. The glass composition was  $\text{SiO}_2\text{-GeO}_2\text{-P}_2\text{O}_5$  for the core and pure  $\text{SiO}_2$  for the cladding with low impurity content. The fiber core diameter, the beam spot size, and the refractive index difference were  $8\ \mu\text{m}$ ,  $5\ \mu\text{m}$ , and  $0.3\%$ , respectively, at a wavelength of  $1.55\ \mu\text{m}$ . To obtain efficient coupling between the diode laser and fiber in a previous study, hemispherical fiber lenses with a short taper length and a large taper angle with a small radius of curvature were required. One of the convenient methods of producing short taper lengths and large taper angles in hemispherical fiber lenses has been reported.

In this chapter, the THEF was redesigned with a longer taper length and a smaller taper angle with a small radius of curvature than the hemispherical fiber lens. The THEFs were fabricated by etching the fiber end in a  $55\%$  HF solution placed in a teflon beaker, with a thin layer of oil floating on top, as shown in Fig. 13. Fig. 13 is a sketched diagram of the etching process; up to 200 fibers may be etched simultaneously in the experiment. The etching process at room temperature in the HF/oil solution was terminated after 25 min. The oil on top of the HF solution has the effect of reducing the fiber etching above the bath surface from the HF vaporization. The higher-density oil floating on the surface of the HF solution reduces the fiber etching caused by the re-deposition of the evaporated HF molecules. In this process, the longer taper length and the smaller taper angle of the fiber end were achieved by controlling the density of the oil floating on top of the HF solution.

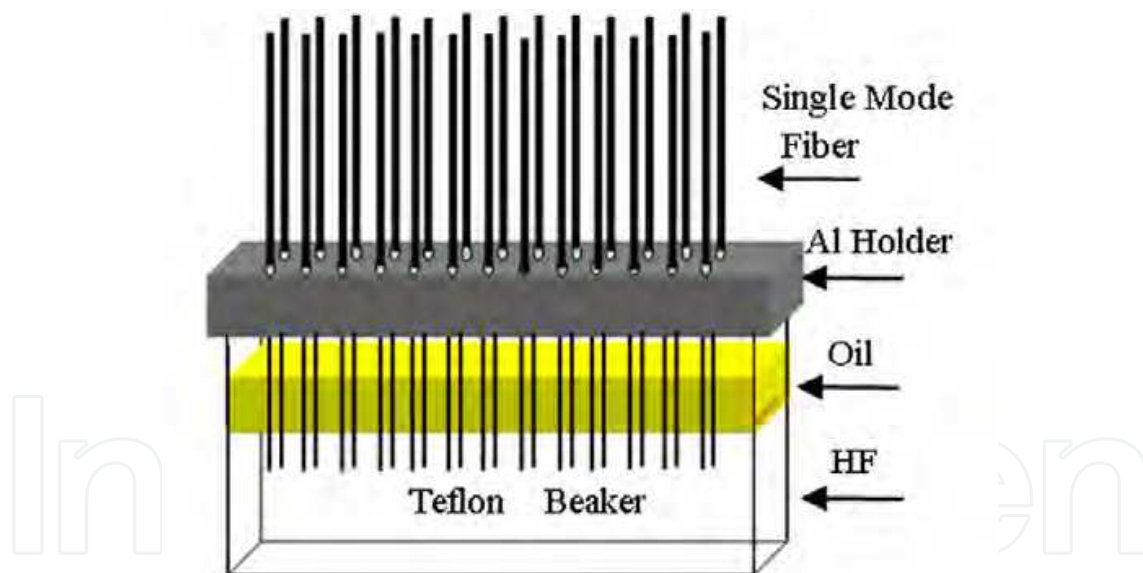


Fig. 13. Setup of the THEF fabrication diagram with the HF solution, oil layer, holder, and the fibers.

The experimental measurements and numerical calculations for the dependence of taper angle on oil density for the THEF are presented. The etching process at room temperature in HF with oil solution was terminated at 25 min. Different densities of oil floating on the HF solution were investigated. The oil density was defined by weight per volume ( $\text{g}/\text{cm}^3$ ). Fig. 14 shows the taper angle as a function of the oil density. This result shows that the taper angle is dependent on the oil density. The oil floating on the HF with an oil solution with lower density and much etching effect caused by HF deposition due to

vaporization exhibits a smaller taper angle. In order to create hyperbolic microlenses for high-coupling efficiency, straight tapers without lateral offsets were required. This was achieved by exactly aligning the fiber vertically with the surface of the HF solution in the fiber holder, as shown in Fig. 13. After the fiber was etched to the desired tapered shape, a hyperbolic microlens for the THEF was formed by heating the fiber tip in a fusion splicer. Only one tapered fiber can be processed with a splicing machine at a time to form a lensed fiber. The duration of the arc discharge and the offset distance between the tapered fiber tip and the arc discharge line were optimized to obtain the proper melting temperatures. In addition, the arcings were performed twice and oriented orthogonally from each other to achieve a symmetrically hyperbolic microlens. A 300- $\mu\text{m}$ -long InGaAsP/InP multi-quantum-well, ridge-waveguide Fabry-Perot laser diode wire bonded on a sub-carrier was used as the gain medium for the fiber gating laser. The FP laser diode, which has a 90% HR coating at the back facet and a low-cost AR-coated front facet of 0.5%, was mounted on a TE cooler to control the substrate temperature. The FP laser beam has a far-field divergence of  $20^\circ \times 30^\circ$  (lateral  $\times$  vertical).

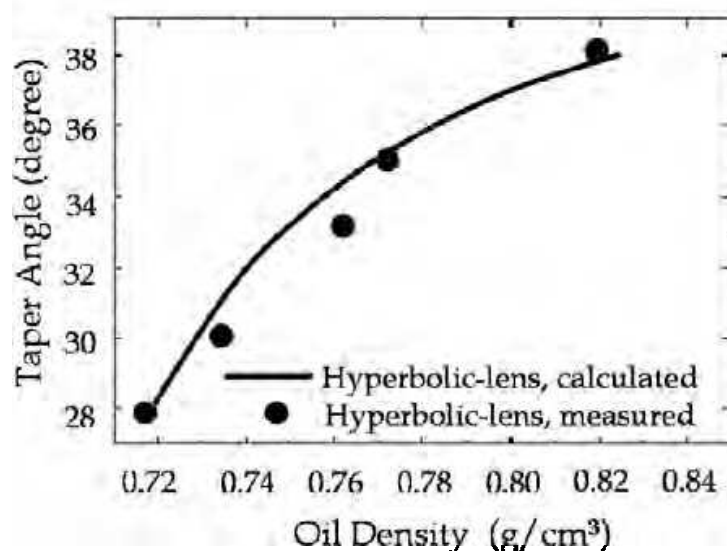


Fig. 14. The taper angle as a function of the local oil density. The taper angle is dependent on the oil density.

### 3.1 Measurements of hyperbolic-end and hemispheric-end microlenses

Fig. 15 shows the hemispherical-end microlens and hyperbolic-end microlens with singular tapered angle by different etching process and fusion parameters. The taper angle of the hemispherical-end microlens and hyperbolic-end microlens are  $2\theta_{\text{hs}}$  and  $2\theta_{\text{hp1}}$ , respectively. The feature of the hyperbolic-end microlens has a smaller taper angle, i.e.  $2\theta_{\text{hp1}} < 2\theta_{\text{hs}}$ , and  $2\theta_{\text{hp2}}$  larger than  $2\theta_{\text{hp1}}$  is necessary. In Figs. 15(a) and (b), both microlenses have a radius of curvature of  $9.4 \mu\text{m}$ . The coupling efficiency of the hemispherical-end microlens and hyperbolic-end microlens as a function of the lenses radius of curvature is shown in Fig. 4. The distance  $L$  between the laser and the fiber lens was optimized at every point for a maximum coupling efficiency. The high coupling performance of microlenses with a hyperbolic profile was due to the improved mode matching and the better wavefront matching between the laser and the fiber compared with the currently available

hemispherical microlenses, which have a typical coupling efficiency of 50%. The radius of the hyperbolic microlens will determine the collimated beam size for mode-size matching, and the hyperbolic shape will remove the hemispherical aberration for wave front matching between the propagating laser beam and the fiber mode. This hyperbolic-end microlens exhibited a better coupling performance compared to other microlenses fabricated by chemical etching and drawn-tapered fiber techniques, which showed a maximum coupling efficiency of 65% for a laser diode with an aspect ratio of 1:1.5. Some previous studies used complicated processes. The lens shape of a perfect THEF was modeled by a hyperbolic curve, is expressed as Eq.(4).

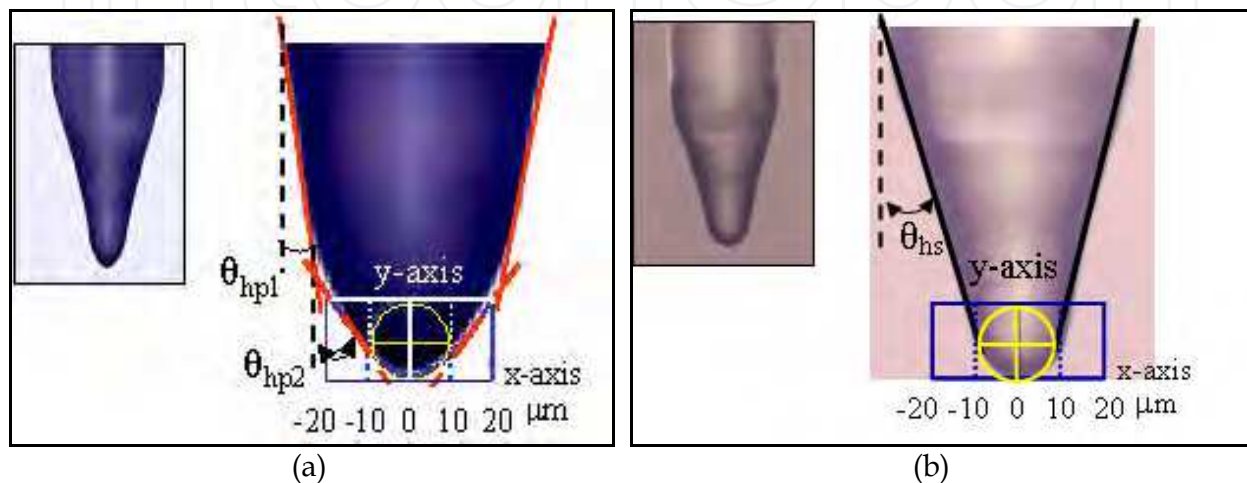


Fig. 15. (a) Hyperbolic-end microlens, and (b) hemispherical-end microlens with different tapered angles. Both microlenses have a radius of curvature of  $9.4 \mu\text{m}$ .

### 3.2 An empirical model for taper length depending on oil density

The HF with oil solution can be divided into three layers: the bottom layer of uncontaminated HF solution, the interface layer of HF with oil solution, and the top-most layer of oil, as shown in Fig. 16(a). Fig. 16(b) shows the etching processes of tapered fiber. The oil floating on top of the HF solution decreases the vaporization effect from the HF solution onto the fiber surface above the HF solution during etching. The local oil density,  $\gamma(\varepsilon)$ , is assumed to vary in the  $\varepsilon$ -direction.

According to Fig. 16(a), the layers I, II, and III are the fiber dipped in the uncontaminated HF solution, the interface layer between the oil layer and the HF solution, and oil layer, respectively. Therefore, the local oil density in layers I, II, and III are zero, a function of  $\varepsilon$ , and a constant (depending on the oil), respectively. The fiber in layer I can be etched to a long round stick, while the fiber in layer II can be etched to form a longer taper length and a smaller taper angle. The etching process in both layers I and II is terminated at room temperature after 25 min. The local oil density,  $\gamma(\varepsilon)$ , in three different layers can be expressed as

$$\gamma(\varepsilon) = \begin{cases} \text{constant} & \varepsilon_1 < \varepsilon \\ [p + q \gamma(\varepsilon)](\varepsilon - \varepsilon_0) & \varepsilon_0 < \varepsilon < \varepsilon_1 \\ 0 & \varepsilon < \varepsilon_0 \end{cases} \quad (16)$$

where the  $p$  and  $q$  are constants. Based on Fig. 16, the taper angle,  $\theta_t$ , is given by

$$\theta_t = 0.5 \tan^{-1}(d_f/2\varepsilon) \tag{17}$$

where the  $d_f$  is the fiber diameter of 125  $\mu\text{m}$ . From Eqs. (16) and (17) yields

$$\theta_t = 0.5 \tan^{-1}\{d_f[p + q\gamma(\varepsilon)]/2\gamma(\varepsilon)\} \tag{18}$$

where the constants  $p$  and  $q$  are  $-0.113$  and  $0.169$ , respectively. The constants  $p$  and  $q$  are from the experimental values of the taper angle related to the oil density. To complete the etching process, the long round stick in layer I disappeared and left a longer taper fiber, as shown in Fig. 17. Figs. 17(a) and 17(b) show the pictures of different etching time, 18 min. and 25 min., respectively. Figure 17(c) shows a tapered fiber picture after completing an etching process to be enlarged by 500 times by SEM (Scanning Electron Micrograph Image). The taper angles are dependent on etching time and oil thickness, as shown in Fig. 18. In the interface region, the fiber was subjected to the influence of adhesive force (horizontal direction) except for surface tension (vertical direction). The activity of the horizontal direction and the vertical direction were  $r_{OH} \sin\theta$  and  $r_{OF} = r_{HF} - r_{OH} \cos\theta$ , respectively. The dependence of the taper length and the taper angle between the hemispherical microlenses and THEFs is shown in Fig. 19.

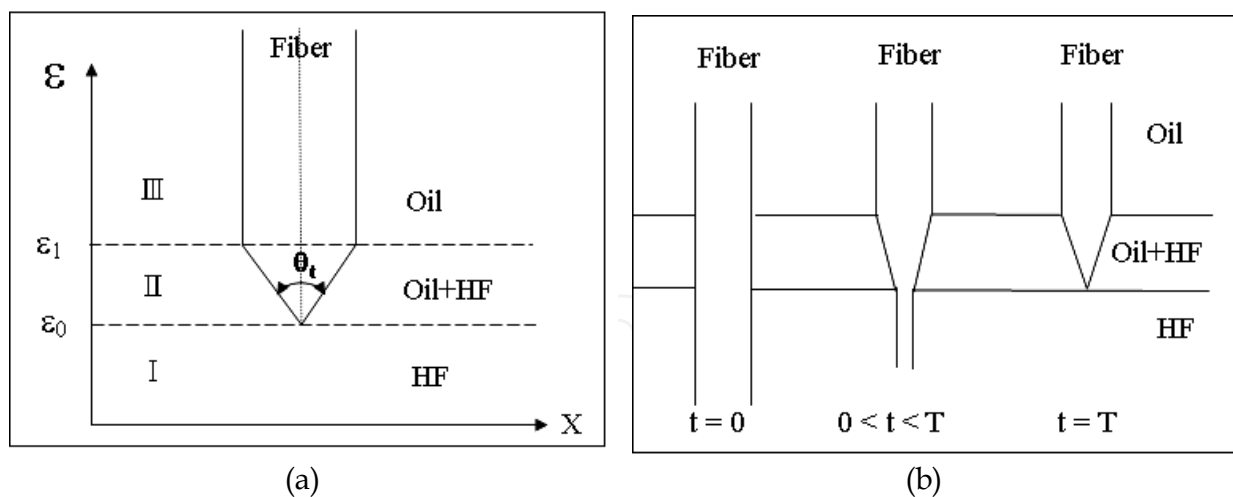


Fig. 16. (a) HF with oil solution divided into three layers; layer I: the fiber dipped in the uncontaminated HF solution, layer II: the interface layer between the oil layer and the HF solution, and layer III: oil layer. (b) Etching processes of fiber microlens at different etching time.

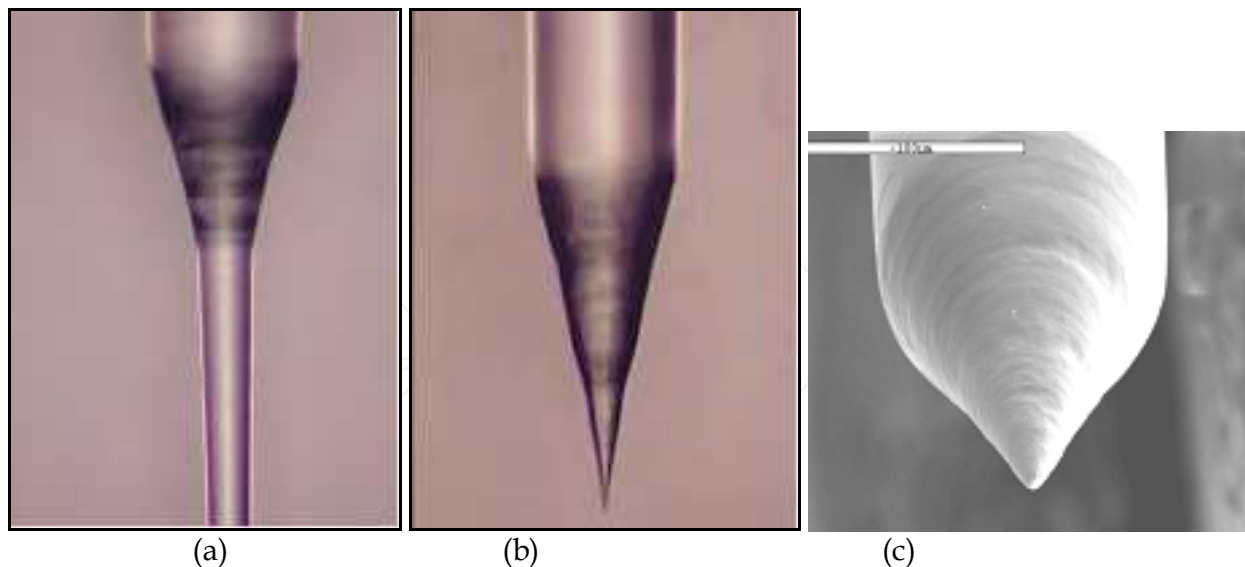


Fig. 17. Pictures of different etching time, (a) 18 min. (b) 25 min., and (c) enlarged by 500 times taper fiber after etching process, photo by SEM (Scanning Electron Micrograph Image).

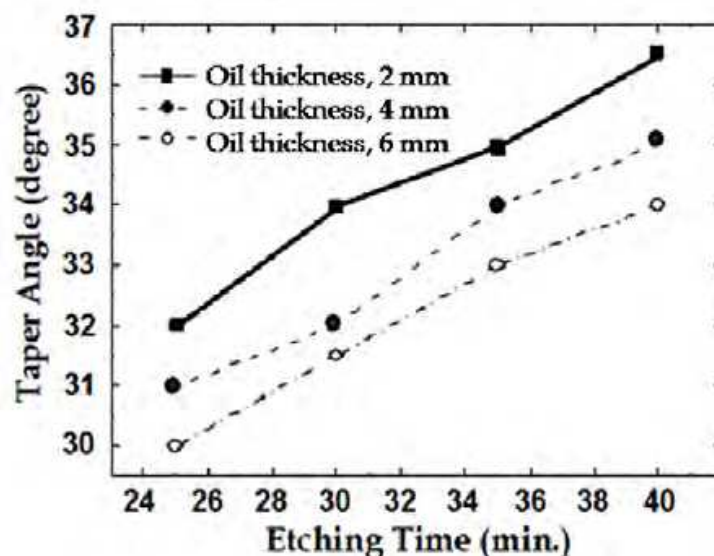


Fig. 18. The taper angles are dependent on etching time and oil thickness.

#### 4. Fabrication of fiber gratings laser with uncoated microlenses

In densely spaced wavelength-routed and large-capacity optical network systems, single-mode lasers with narrow linewidth and low temperature sensitivity are of particular importance as the light sources in transmitter modules. Using a temperature-insensitive and low-chirp fiber Bragg grating reflector as the external cavity for the semiconductor gain element, fiber grating external cavity lasers (FGECLs) have been developed for 2.5 Gbit/s or 10 Gbit/s WDM with a low bit error rate penalty. It has been shown that the side-mode suppression ratio (SMSR) of the non-AR-coated FGECL exhibits a current-dependent oscillation. To avoid the formation of an intra cavity and increase the SMSR, Morton et al.

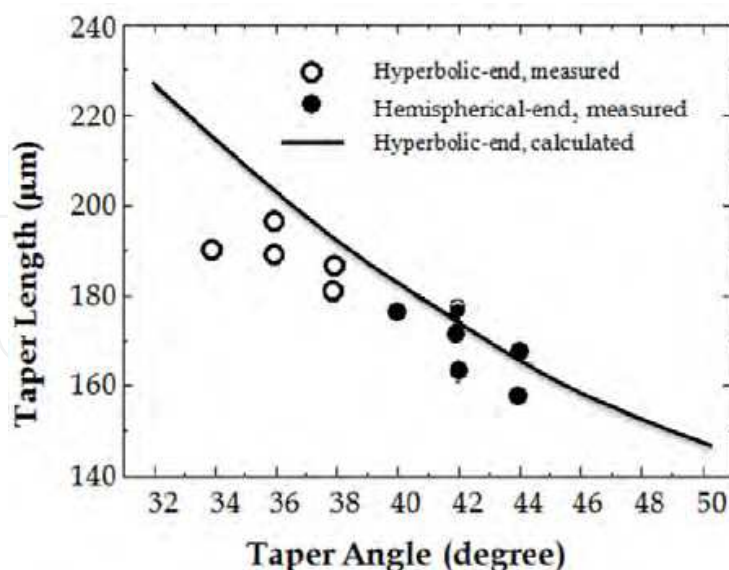


Fig. 19. The dependence of taper length and taper angle between the hemispherical microlenses and THEFs.

have demonstrated an FGECL configuration by applying antireflection (AR) coatings to both the fiber tip and the diode laser front facet (facet closest to fiber tip). However, both the fiber tip and the diode laser front facet required low AR coatings ( $1 \times 10^{-5}$ ). This makes the fabrication process complicated and causes an increase in the cost of the production. Therefore, compact integration of the diode laser and the fiber grating external cavity, which would allow the ease of optical coating and the reduction of back reflection from the fiber tip, is of great research interest for optimizing the FGECL performance. A fiber microlens which provides an efficient coupling mechanism to match the spot size of the diode laser to the fiber is commonly used for optical alignment in FGECL modules.

This paragraph will elucidate the fabrication of a fiber grating external cavity laser (FGECL) module with a low cost while still maintaining a good performance using a low-cost AR (Anti-reflection)-coated ( $5 \times 10^{-3}$ ) laser and a tapered hyperbolic-end fiber (THEF) microlens. Previously, high-performance FGECL modules have only been available by using a complicated AR-coated ( $1 \times 10^{-5}$ ) laser process that leads to a high packaging cost. Our FGECL consisted of a HR/AR-coated diode laser, a THEF microlens, and a fiber grating. The results showed that the FGECL module exhibits a side-mode suppression ratio (SMSR) higher than 44 dB, a higher output power of more than 2 mW, and a larger operation current range of over 50 mA. In addition, excellent wavelength stability and a low-penalty directly modulated 2.488 Gbit/s were also obtained for FGECL modules. The THEF microlens demonstrated up to 86% coupling efficiency for a laser with an aspect ratio of 1:1.5. Low-cost FGECL modules with good performance were achieved primarily owing to the THEF microlens having a high coupling efficiency (typically 75%) which enhanced the feedback power from the fiber grating external cavity to the HR/AR-coated laser compared with the currently available hemispherical microlens which has low coupling efficiency (typically 50%). Therefore, the packaged FGECL module is suitable for use in low cost 2.5 Gbit/s lightwave transmission systems.

#### 4.1 Fiber grating external cavity laser structure

The fiber grating used in the FGECL comprises a single-mode fiber grating, and an uncoated THEF microlens. They are fabricated on the same photosensitive single-mode fiber with a mode-field diameter of  $9.6 \mu\text{m}$  at  $\lambda = 1.55 \mu\text{m}$ . The fiber Bragg grating is firstly written on the photosensitive single-mode fiber using 248 nm UV light. The 6-mm-long grating is formed in the core of germanium-doped silica glass. To stabilize the grating formation, thermal annealing at  $140^\circ\text{C}$  was performed for 40 h. After the preparation and characterization of the fiber grating, the THEF microlens was processed at the tip of the single-mode fiber with the grating formation. To conveniently fabricate the high coupling efficiency THEF microlens, a unique chemical etching and fusing technique was developed. According to the abovementioned, the THEF were fabricated by symmetrically tapering the fiber during etching and hyperbolically lensing the tip during fusing process. For a high coupling efficiency between the diode laser and the single-mode fiber grating, the THEF microlenses are required to have a small radius of curvature and a low lateral offset between the microlens center and the fiber axis.

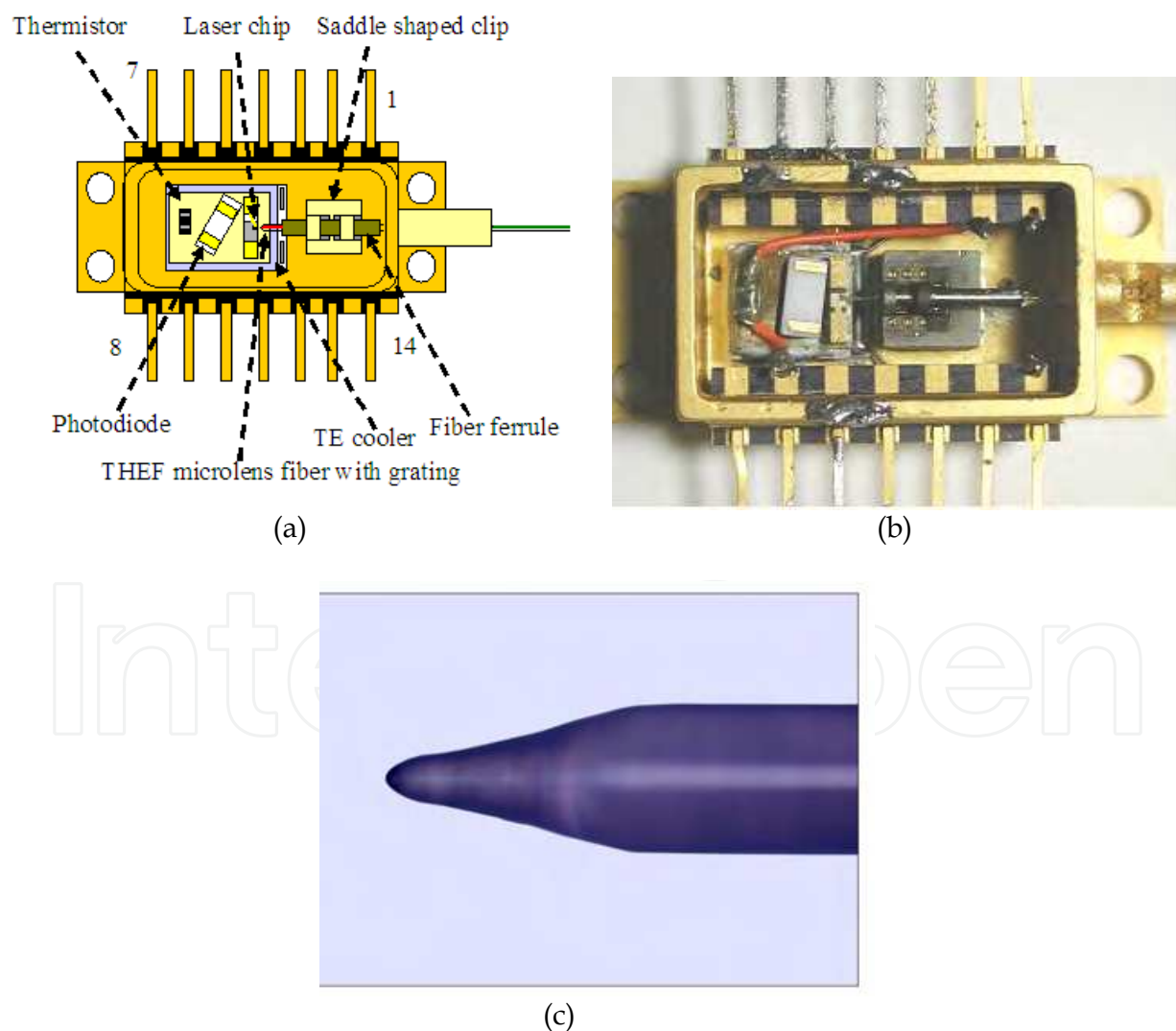


Fig. 20. (a) AR-coated FGECL module, (b) laser-welded butterfly-type FGECL module, and (c) THEF microlens.

Fig. 20 shows the FGECL module configuration. The FGECL module consisted of an HR/AR-coated diode laser, a THEF microlens, a fiber grating, a photodiode, and a TE cooler, as shown in Fig. 20(a). A laser-welded butterfly-type FGECL module package is shown in Fig. 20(b). A 300- $\mu\text{m}$ -long InGaAsP/InP multi-quantum-well, ridge-waveguide Fabry-Perot laser diode wire-bonded on a sub-carrier was used as the gain medium for the FGECL. The FP laser diode which has a 90% HR coating at the back facet, and a low-cost AR-coated front facet of 0.5%, was mounted on a TE cooler to control the substrate temperature. The FP laser beam has a far-field divergence of  $20^\circ \times 30^\circ$  (lateral  $\times$  vertical). The fiber grating with the THEF microlens was assembled in a fiber ferrule, and then the FGECL module was packaged by laser welding technique, as shown in Fig. 20(b). Fig. 20(c) shows a THEF microlens.

#### 4.2 Performance of the fiber grating external cavity laser

For each THEF, the maximum coupling efficiency between the laser diode and the fiber was measured. The coupling efficiency is defined as the ratio of the optical power from a 2-m-long fiber pigtail with a THEF to that of the FP laser output power. When the maximum coupling was achieved, the distance between the front facet of the laser and the tapered hyperbolic-end fiber tip was 9  $\mu\text{m}$ . The 3 dB lateral alignment tolerance between the laser and the fiber was  $\pm 1.0 \mu\text{m}$ . The apodized fiber grating has a reflectivity of 50% at a center wavelength of 1539.15 nm, and a 3 dB bandwidth of 0.2 nm. The spectra of non-AR-coated and AR-coated FP laser diodes are shown in Figs. 21(a) and 21(b), respectively, at a substrate temperature of 25°C. The non-AR-coated and AR-coated Fabry-Perot laser diodes, and FGECL module typically exhibit linear L-I curves up to a pumping current of more than 70 mA, as shown in Fig. 22(a). In the Fig. 22(a), the threshold current ( $I_{\text{th}}$ ) of the non-AR-coated laser, AR-coated laser, and FGECL were 12 mA, 32 mA, and 18 mA, respectively, at a substrate temperature of 25°C. At an operation current of 70 mA, the output powers of the non-AR-coated laser, AR-coated laser, and FGECL were more than 14 mW, 7 mW, and 5 mW, respectively. In the Fig. 22(a), the FGECL module has a lower threshold current and slope efficiency than the AR-coated laser. The spectral characteristics of the FGECL module can be analyzed as a single-cavity laser formed by a HR back facet and an effective front facet from the reflectivity and coupling efficiency of the fiber grating external cavity.

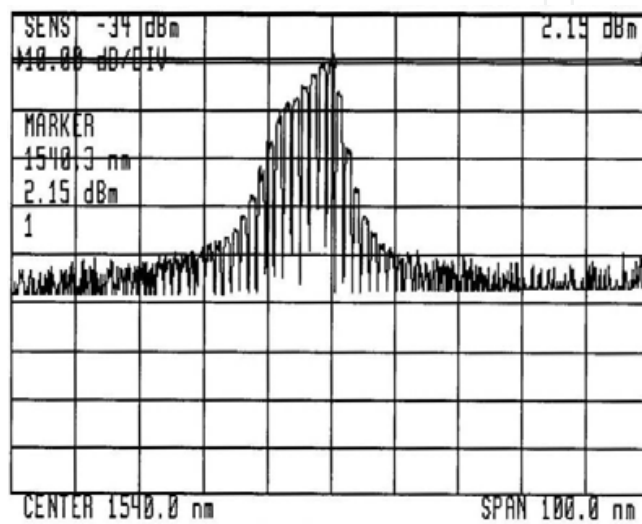
The  $m$ th mode effective reflectivity  $R_{2s}$  at the diode laser front facet, including all the reflection components from the output end of the FGECL is given by

$$R_{2s} = |r_{2s}|^2 = \left| r_2 + (1 - |r_2|^2) r_{2ext} \exp(-j2\pi\nu_m \tau_{ext}) \right|^2 \quad (19)$$

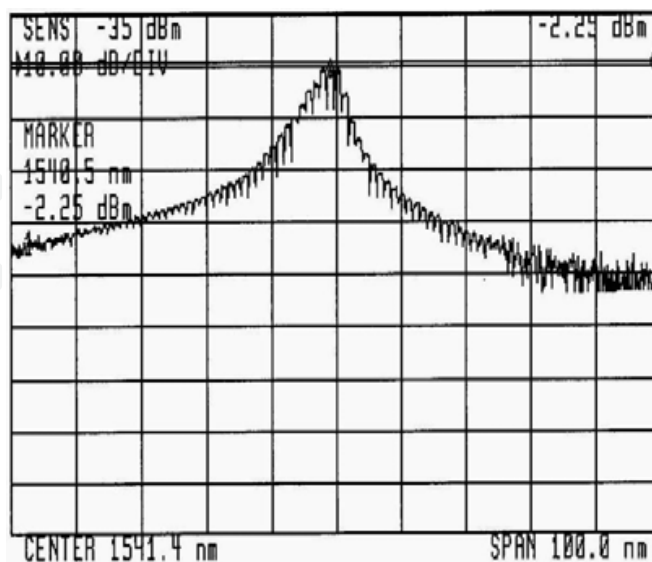
where  $r_2$ ,  $r_{2ext}$ ,  $\nu_m$ , and  $\tau_{ext}$  are the reflection coefficient of the diode laser front facet, the external cavity reflection coefficient, the optical frequency, and the round-trip delay through the length of the external cavity, respectively. Here, the external cavity length is the distance from the laser diode front-facet to the center of the fiber grating. For the longitudinal mode of the wavelength located within the 3 dB bandwidth of the fiber grating reflection, the value of  $r_{2ext}$  can be estimated by taking into account the fiber grating reflectivity  $R_g$  and the coupling efficiency  $\eta$ , and is given by

$$R_{2ext} = |r_{2ext}|^2 = \eta^2 R_g \quad (20)$$

The effective reflectivity  $R_{2s}$  has a higher value for the case of higher  $R_g$  and  $\eta$ . However, for the FGECL,  $R_{2s}$  is lower than the reflectivity of the natural cleavage facet. Therefore, the mirror loss of the equivalent cavity is higher. The lower slope efficiency of the FGECL may be induced by the internal refractive loss of the fiber grating, due to the imperfect refractive index modulation and uncoated section of the grating. Fig. 22(b) shows the lasing spectrum with an SMSR of more than 44 dB at a substrate temperature of 25°C and an injection current of 40 mA.



(a)



(b)

Fig. 21. Spectra of (a) non-AR-coated and (b) AR-coated FP laser diodes at substrate temperature of 25°C.

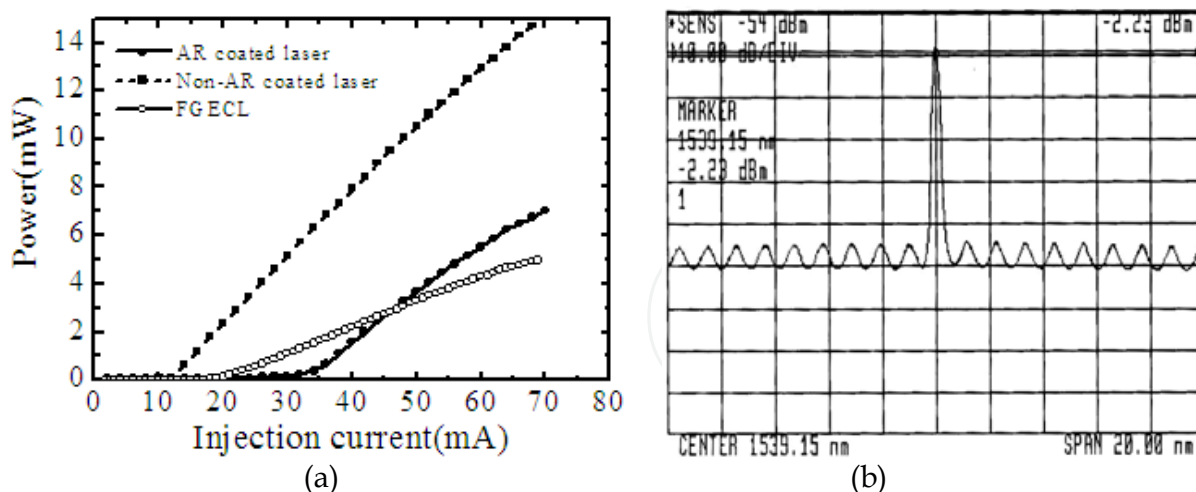


Fig. 22. (a) Typical L-I characteristics of AR-coated laser, non-AR-coated laser, and FGECL module at substrate temperature of 25°C and (b) lasing spectrum of FGECL module with SMSR of more than 44 dB at substrate temperature of 25°C and an injection current of 40 mA.

The lasing peak wavelength ( $\lambda_o$ ) and the SMSR of the AR-coated FGECL as a function of current (I) is shown in Fig. 23. In the range of current from 18 to 70 mA at an ambient temperature of 28°C,  $\lambda_o$  of the AR-coated FGECL is almost fixed at 1539.15 nm, which is consistent with the center wavelength of the fiber grating. This indicates that for wavelength stability, the operation current range of the AR-coated FGECL is tenfold that of the non-AR-coated FGECL. At a substrate temperature of 25°C, the AR-coated FGECL maintains a single longitudinal mode operation with the SMSR mostly greater than 44 dB at operation currents from 30 to 60 mA, as shown in Fig. 23. The high values of the SMSR indicate that the main mode is strongly locked by the fiber grating's external cavity.

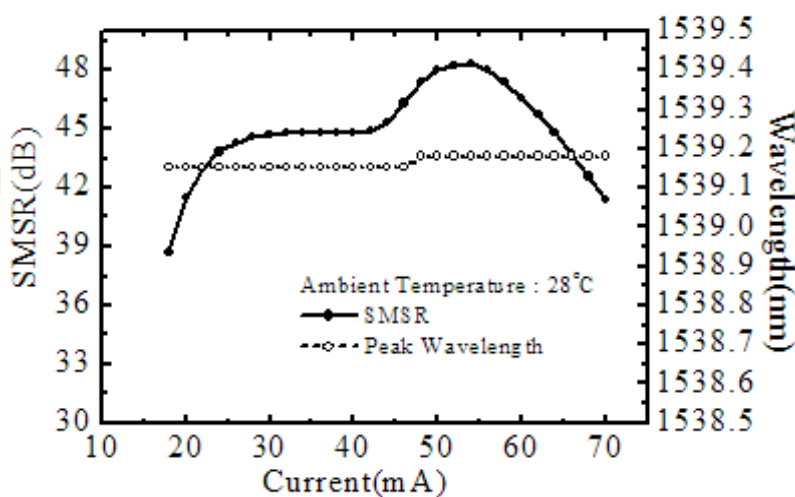


Fig. 23. Lasing peak wavelengths ( $\lambda_o$ 's) and SMSR of AR-coated FGECL as a function of pumping current at substrate temperature of 25°C.

The lasing peak wavelength ( $\lambda_o$ ) and SMSR of the AR-coated FGECL as a function of temperature (T) are shown in Fig. 24. The lasing peak wavelength is strongly locked by the

fiber grating and is dominated by the fiber grating. The  $\lambda_o$  is dependent on lasing wavelength of fiber grating temperature at ambient temperature of 28°C. The temperature of the laser chip is controlled using a TE cooler. To determine the effect of temperature on the SMSR and  $\lambda_o$ , the data was measured at  $I = 40$  mA. The AR-coated FGECL had a high SMSR at temperatures from 20 to 40°C. At 20 to 40°C, the SMSR varies from 38.5 to 47.4 dB, as shown in Fig. 24. This change of SMSR was caused by the temperature-induced red shift of the diode laser gain spectrum. The FGECL module showed excellent single-longitudinal-mode characteristics. In the range of temperatures from 20 to 40°C, little variation of  $\lambda_o$  was observed. The average variation of  $\Delta\lambda/\Delta T$  was  $\sim 0.0042$  nm/°C, and the shift of  $\lambda_o$  was within the 3 dB window of the fiber grating.

On the other hand, for the temperature dependence of the non-AR-coated FGECL, the peak wavelength ( $\lambda_o$ ) has more significant variations between 1536 to 1545.8 nm at 18 to 36°C, as shown in Fig. 25. The FGECL with a non-AR-coated laser operates less effectively in a single mode from the measured SMSRs. This is due to the mode hopping caused by the strong intra-cavity resonance of the FP diode laser. While the lasing mode of the FP diode laser is outside the 3dB window of the fiber grating, there is no more mode selection by the external cavity. Fig. 26 shows a plot of the SMSR and  $\lambda_o$  as a function of the pumping current of the non-AR-coated FGECL at a substrate temperature of 25°C. The  $\lambda_o$  showed current-dependent variation, and weak wavelength selection by the fiber grating external cavity. The SMSR exhibited current-dependent oscillations with a short operation current range from 17 to 22 mA. Without AR coating on the diode laser's front facet, the FGECL shows a nonlinear L-I curve and a low SMSR, indicating strong mode hopping competed by the diode-laser FP cavity and the external cavity.

Fig. 27 shows the BER performance of the AR-coated and non-AR-coated FGECL modules with a transmission rate of 2.488 Gbit/s. The measured conditions were a NRZ format, 2<sup>23</sup>-1 pseudo-random binary sequence (PRBS) pattern, with a modulation current of 20 mA, and an operation current of 40 mA at substrate temperature of 25°C. The power penalties of the AR-coated and non-AR-coated FGECL modules for 25 km SMF (ITU G.652) were measured at 0.8 and 1.42 dB, respectively. The AR-coated FGECL module shows much better BER performance than the non-AR-coated FGECL module. Therefore, the packaged FGECL module is suitable for use in low cost 2.5 Gbit/s lightwave transmission systems.

## 5. Discussion and conclusions

In general, a high-performance FGECL requires a low AR-coated ( $1 \times 10^{-5}$ ) laser. However, such packages require complicated processes, which make their cost too high. In this chapter, the experimental results demonstrate the possibility fabricating FGECL modules at low cost while still maintaining a good performance by employing a low-cost AR-coated ( $5 \times 10^{-3}$ ) laser and a THEF microlens. Compared with previous studies, new low-cost FGECL modules exhibited a better SMSR ( $>44$  dB), a good wavelength stability (almost fixed from 18~70 mA), and an excellent temperature stability ( $\Delta\lambda/\Delta T \sim 0.0042$  nm/°C). In a previous study, an FGECL showed a higher SMSR ( $>55$  dB) and a better wavelength stability ( $\Delta\lambda/\Delta I \sim 0.0062$  nm/mA from 8~250 mA), however, both the fiber tip and the diode laser's front facet required a low-AR coating ( $1 \times 10^{-5}$ ). This makes the fabrication process complicated and causes a rise in the cost of the production. In this chapter, low-cost FGECL modules with good performance were achieved primarily owing to the THEF microlenses having a high coupling efficiency (typically 75%) which enhances the feedback power from

the fiber grating external cavity to the HR/AR-coated laser compared with the currently available hemispherical microlens which has a low coupling efficiency (typically 50%). In addition, the experimental results demonstrated a good performance of the BER and a low penalty of directly modulated 2.488 Gbit/s for FGECL modules with HR/AR-coated diode lasers and uncoated THEF microlenses. This clearly indicates that the packaged FGECL modules are suitable for use in low-cost 2.5 Gbit/s lightwave transmission systems, such as gigabit passive optical networks (GPONs), metropolitan area networks (MANs), and fiber-to-the-home (FTTH) applications.

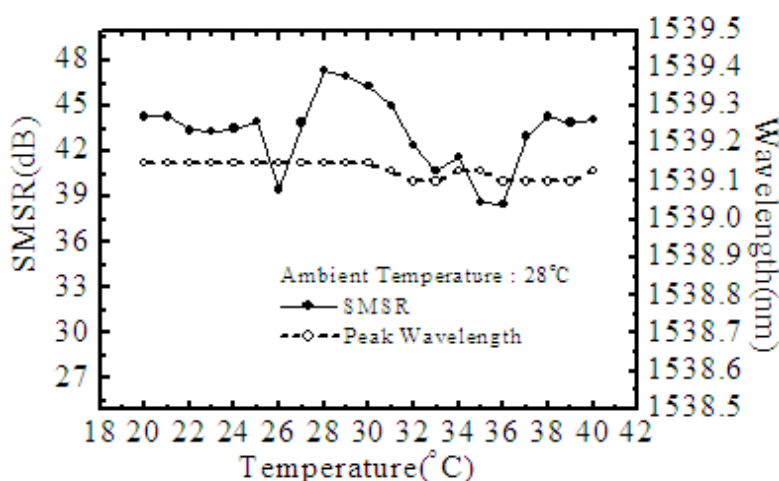


Fig. 24. Lasing peak wavelengths ( $\lambda_o$ ) and SMSR of AR-coated FGECL module as a function of temperature at the injection current of 40 mA. The peak wavelength is dependent on lasing wavelength on fiber grating temperature at ambient temperature of 28°C.

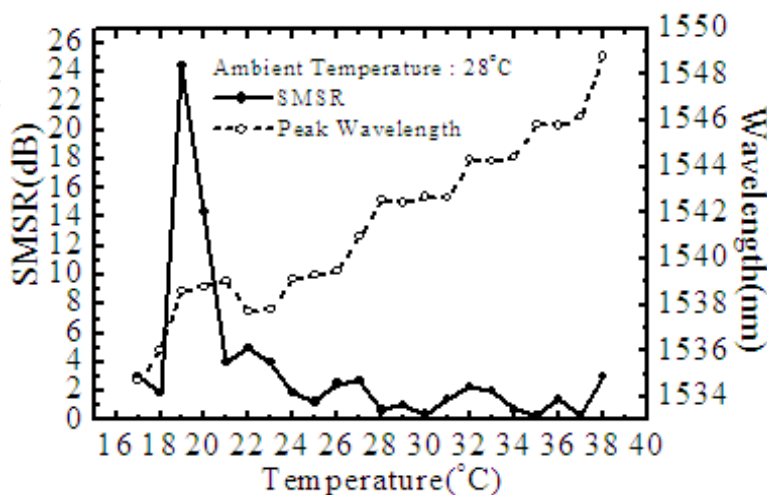


Fig. 25. Lasing peak wavelength ( $\lambda_o$ ) and SMSR of non-AR-coated FGECL module as a function of temperature at the injection current of 40 mA.

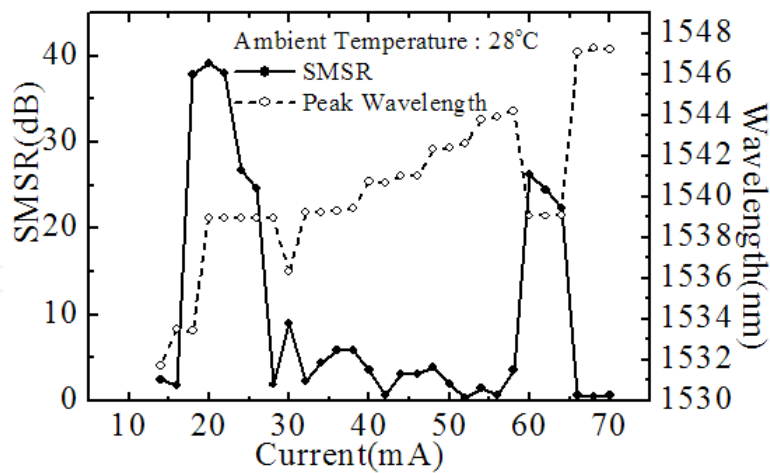


Fig. 26. Lasing peak wavelength ( $\lambda_0$ ) and SMSR of non-AR-coated FGECL module as a function of injection current at substrate temperature of 25°C.

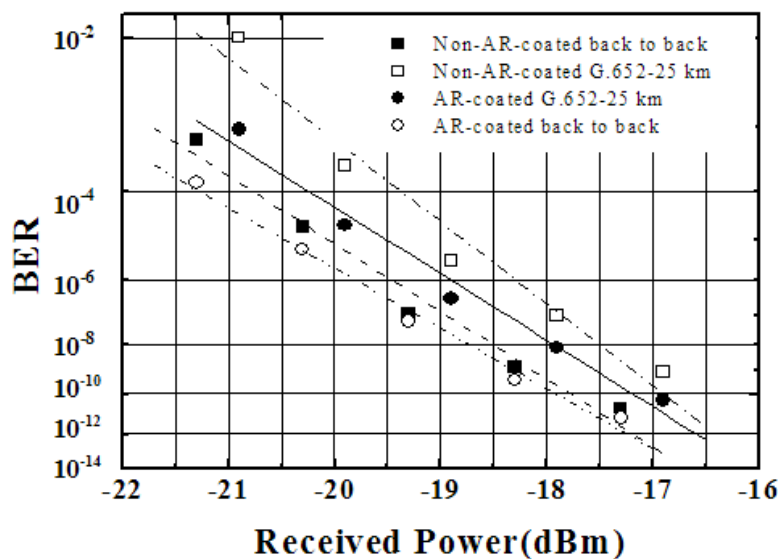


Fig. 27. BER performance of AR-coated and non-AR-coated FGECL modules with a transmission rate of 2.488 Gbit/s.

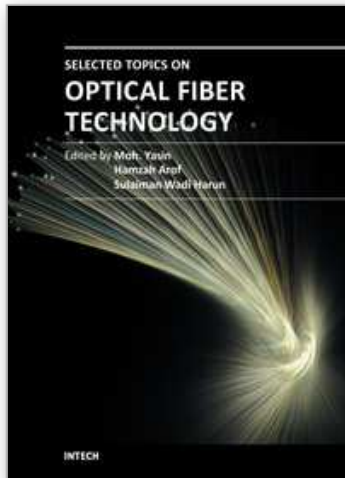
## 6. References

- ASAP™ (Advanced Systems Analysis Program), Breault Research Organization, Inc., Tucson, Arizona USA
- Yang, H. and et al. (2010). Investigation of the efficient coupling between a highly elliptical Gaussian profile output from a laser diode and a single mode fiber using a hyperbolic-shaped microlens, *Optics & Laser Technology*, Vol.42, No. 6, pp.918-926
- Hillerich, B. and Guttman J. (1989). Deterioration of taper lens performance due to taper asymmetry, *J. Lightwave Technol.* No. 7, pp. 99-104
- Mathyssek, K. and et al. (1985). Fabrication and investigation of drawn fiber tapers with spherical microlenses, *J. Opt. Commun.* No.6, pp. 142-146

- Edwards, C. and et al. (1993). Ideal microlenses for laser to fiber coupling, *J. Lightwave Technol.* No.11, pp. 252-257
- Gangopadhyay, S. and Sarkar, S. (1997). ABCD matrix for reflection and refraction of Gaussian light beams at surfaces of hyperboloid of revolution and efficiency computation for laser diode to single-mode fiber coupling by way of a hyperbolic lens on the fiber tip, *Appl. Opt.* Vol. 36, pp. 8582-8586
- Presby, H. and et al. (1990). Laser micromachining of efficient fiber microlenses, *Appl. Opt.* Vol. 29, pp. 2692-2695.
- Goodman, J. (2005). Introduction to Fourier optics, Roberts & Company Publishers, pp. 63-126. ISBN 0-9747077-2-4, Colorado, USA
- Yariv, A., (1996). Optical Electronics in Modern Communications, fifth edition, Oxford Univ. Press, pp. 52-53, ISBN 0-19-510626-1, New York, USA
- Kogelink, H., (1964). Coupling and conversion coefficients for optical modes in quasi-optics, Microwave Research Institute Symposia Series, Polytechnic Press, New York, Vol.14, pp. 333-347
- Mathyssek K, and et al. (1985). Fabrication and investigation of drawn fiber tapers with spherical microlenses, *J. Opt. Commun.* No. 6, pp. 142-146
- Hillerich, B. and Guttman, J. (1989). Deterioration of taper lens performance due to taper asymmetry, *J. Lightwave Technol.*, Vol. 7, pp. 99-104
- Lay, T., and et al. (2002). 1.55- $\mu\text{m}$  Non-anti-reflection-coated Fiber Grating Laser for Single-longitudinal Mode Operation, *Opt. Quantum Electron.* Vol. 34, pp. pp. 687-696
- Morton, P. and et al. (1994). Stable single mode hybrid laser with high power and narrow linewidth, *Appl. Phys. Lett.*, Vol. 64, pp. 2634-2636
- Yang, H. and et al. (2004). High coupling tapered hyperbolic fiber microlens and taper asymmetry effect, *IEEE J. Lightwave Technol.* Vol. 22, No. 5, pp. 1395-1401
- Petermann, K. (1988). *Laser Diode Modulation and Noise*, Kluwer Academic Publishers, Chap. 2&9, ISBN 90-277-2672-8, Tokyo, Japan
- Hill, K., and et al. (1993). Bragg gratings fabricated in monomode photosensitive optical fiber by UV exposure through a phase mask, *Appl. Phys Lett.* vol. 62, pp. 1035-1037
- Lemaire, P. and et al. (1993). High pressure H<sub>2</sub> loading as a technique for achieving ultrahigh UV photosensitivity and thermal sensitivity in GeO<sub>2</sub> doped optical fibres, *Electron Lett.*, Vol. 29, no. 13, pp. 1191-1193
- Lay, T., and et al. (2003). 1.55- $\mu\text{m}$  Fiber grating laser utilizing an uncoated tapered hemispherical-end fiber microlens, *J. Appl. Phys.* Vol. 42, Part 1, No. 2A, pp. 1-3
- Sigg, J. (1993). Effects of optical feedback on the light-current characteristics of semiconductor lasers, *IEEE J. Quantum Electron.*, Vol. 29, No. 5, pp.1262-1270
- Kallimani, K. and O'mahony, K. (1998). Calculation of optical power emitted from a fiber grating laser, *IEE Pro-optoelectron*, Vol. 145, No. 6, pp.319-324
- Annovazzi-Lodi, V. and et al. (2000). Power efficiency of a semiconductor laser with an external cavity, *J. Optical Quantum Electron.*, Vol. 32, pp. 1343-1350
- Timofeev, F. and et al. (1995). Spectral characteristics of a reduced cavity singlemode semiconductor fiber grating laser for applications in dense WDM systems, *Proc. 21st European Conf. Optic. Commun. (ECOC'95)*, Brussels, Belgium, paper Tu.P.26, pp. 477-480
- Huang, S. and et al. (2000). High coupling optical design for laser diodes with large aspect ratio, *IEEE Trans. Adv. Packag.*, Vol. 23, pp. 165-169

- Lin, C. (1989). *Optoelectronic technology and lightwave communications systems*, New York: Van Nostrand Reinhold, pp.175-194, ISBN 04-422-6050-4, New York, USA
- Mobarhan, K. and et al. (2002). Laser diode packaging technology: 980 nm EDFA pump lasers for telecommunication applications, Application Note, No. 3, pp. 1-7, Newport Corp., CA, USA
- Yang, H. and et al. (2001). An optimum approach for fabrication of tapered hemispherical-end fiber for laser module packaging," *J. Electron. Mater.*, Vol. 30, pp. 271-274
- Lee, T. and et al. (1982). Short-cavity InGaAsP injection lasers: dependence of mode spectra and single longitudinal mode power on cavity length," *IEEE J. Quantum Electron.*, Vol. QE-18, pp.1101~1112
- Shiraishi, K. and et al. (1995). A fiber lens with a long working distance for integrated coupling between laser diodes and single-mode fibers, *IEEE J. Lightwave Technol.*, Vol. 13, pp. 1736-1744
- Lee, T. and et al. (1982). Short-cavity InGaAsP injection lasers: dependence of mode spectra and single longitudinal mode power on cavity length, *IEEE J. Quantum Electron.*, Vol. QE-18, pp.1101~1112
- Yang, H. and et al. (2007). Low-cost fiber grating laser module package employing a hyperbolic fiber microlens, *J. Appl. Phys.*, Vol. 46, No. 3A, pp. 1016-1020
- Yariv, A. (1973). Coupled-mode theory for guided-wave optics, *IEEE J. Quantum Electron.*, Vol. QE-9, pp. 919~933
- Timofeev, F. and et al. (2000). Experimental and theoretical study of high temperature-stability and low-chirp 1.55 $\mu$ m semiconductor laser with an external fiber grating, *Fiber and Integrated Optics*, Vol. 19, pp. 327-353

IntechOpen



## **Selected Topics on Optical Fiber Technology**

Edited by Dr Moh. Yasin

ISBN 978-953-51-0091-1

Hard cover, 668 pages

**Publisher** InTech

**Published online** 22, February, 2012

**Published in print edition** February, 2012

This book presents a comprehensive account of the recent advances and research in optical fiber technology. It covers a broad spectrum of topics in special areas of optical fiber technology. The book highlights the development of fiber lasers, optical fiber applications in medical, imaging, spectroscopy and measurement, new optical fibers and sensors. This is an essential reference for researchers working in optical fiber researches and for industrial users who need to be aware of current developments in fiber lasers, sensors and other optical fiber applications.

### **How to reference**

In order to correctly reference this scholarly work, feel free to copy and paste the following:

Huei-Min Yang (2012). Design of High Performance and Low-Cost Single Longitudinal Mode Laser Module for DWDM Application, Selected Topics on Optical Fiber Technology, Dr Moh. Yasin (Ed.), ISBN: 978-953-51-0091-1, InTech, Available from: <http://www.intechopen.com/books/selected-topics-on-optical-fiber-technology/design-of-high-performance-and-low-cost-single-longitudinal-mode-laser-module-for-dwdm-application>

**INTECH**  
open science | open minds

### **InTech Europe**

University Campus STeP Ri  
Slavka Krautzeka 83/A  
51000 Rijeka, Croatia  
Phone: +385 (51) 770 447  
Fax: +385 (51) 686 166  
[www.intechopen.com](http://www.intechopen.com)

### **InTech China**

Unit 405, Office Block, Hotel Equatorial Shanghai  
No.65, Yan An Road (West), Shanghai, 200040, China  
中国上海市延安西路65号上海国际贵都大饭店办公楼405单元  
Phone: +86-21-62489820  
Fax: +86-21-62489821

© 2012 The Author(s). Licensee IntechOpen. This is an open access article distributed under the terms of the [Creative Commons Attribution 3.0 License](#), which permits unrestricted use, distribution, and reproduction in any medium, provided the original work is properly cited.

IntechOpen

IntechOpen